FBXL5 Regulates IRP2 Stability in Iron Homeostasis via an Oxygen-Responsive [2Fe2S] Cluster

Hui Wang,[1,2,5] Hui Shi,[1,2,5] Elizabeth R. Canarie,[3] Seoyeon Hong,[3] Matthew F. Bush,[3] Stefan Stoll,[3] Elizabeth A. Leibold,[4] and Ning Zheng[1,2,6,*]

[1]Department of Pharmacology, University of Washington, Seattle, WA 98195, USA

[2]Howard Hughes Medical Institute, University of Washington, Seattle, WA 98195, USA

[3]Department of Chemistry, University of Washington, Seattle, WA 98195, USA

[4]Division of Hematology and Hematologic Malignancies and Molecular Medicine Program, University of Utah, Salt Lake City, UT 84112, USA

[5]These authors contributed equally

[6]Lead Contact

[*]Correspondence: nzheng@uw.edu

Summary

Cellular iron homeostasis is dominated by FBXL5-mediated degradation of iron regulatory protein 2 (IRP2), which is dependent on both iron and oxygen. However, how the physical interaction between FBXL5 and IRP2 is regulated remains elusive. Here we show that the C-terminal substrate-binding domain of FBXL5 harbors a [2Fe2S] cluster in the oxidized state. A cryo-EM structure of the IRP2-FBXL5-SKP1 complex reveals that the cluster organizes the FBXL5 C-terminal loop responsible for recruiting IRP2. Interestingly, IRP2 binding to FBXL5 hinges on the oxidized state of the [2Fe2S] cluster maintained by ambient oxygen, which could explain hypoxia-induced IRP2 stabilization. Steric incompatibility also allows FBXL5 to physically dislodge IRP2 from iron-responsive element-RNA to facilitate its turnover. Taken together, our studies have identified an iron-sulfur cluster within FBXL5, which sensitizes IRP2 polyubiquitination and degradation to both iron and oxygen.

Keywords

FBXL5, iron-sulfur cluster, oxygen-responsive, IRP2, iron homeostasis, cryo-EM

Introduction

Iron, an essential element of most life forms, is widely utilized by a variety of critical biological processes. These include, but are not limited to, respiration, DNA synthesis, oxygen transport, and reactive oxygen species (ROS) sensing (Abbaspour et al., 2014; Lieu et al., 2001). Iron is naturally exploited by the cell through its incorporation into numerous proteins, either directly or via cofactors such as heme and Fe-S clusters (Beard, 2001). Iron deficiency, which impairs the functions of iron-containing proteins, affects billions of people worldwide and leads to cognitive defects in children and anemia in adults. Iron overload, on the other hand, generates reactive radicals that oxidatively damage cellular components and is associated with hemochromatosis and neurodegenerative disorders, including Parkinson's and Alzheimer's diseases (Crielaard et al., 2017). Cellular iron levels, therefore, must be strictly maintained (Hentze et al., 2004; Hentze et al., 2010).

In mammals, cellular iron homeostasis is predominantly regulated at the post-transcriptional level. In response to low iron levels, Iron Regulatory Proteins 1 and 2 (IRP1 and 2) control the expression of a cohort of iron metabolism genes by binding to the iron-responsive elements (IREs) found in their mRNA transcripts (Anderson et al., 2012; Rouault, 2006; Wallander et al., 2006). Interestingly, despite the high sequence homology shared between the two IRPs, their IRE-binding activities are distinctively regulated. IRP1 is switched from an IRE-binding protein to a cytosolic aconitase upon the insertion of a [4Fe4S] cluster, whereas IRP2 is primarily regulated by protein stability. With limiting iron or oxygen, IRP2 is stable and binds IREs. Under iron- and oxygen-enriched conditions, IRP2 undergoes ubiquitin-dependent proteasomal degradation (Guo et al., 1995; Haile et al., 1992; Hanson et al., 1999; Hanson et al., 2003; Iwai et al., 1995).

A decade ago, F-box and leucine-rich repeats protein 5 (FBXL5) was identified as the substrate receptor subunit of an SKP1-CUL1-F box (SCF) ubiquitin ligase complex that specifically recognizes IRP2 and promotes its iron- and oxygen-dependent degradation (Salahudeen et al., 2009; Vashisht et al., 2009). Distinct from other F-box proteins, FBXL5 contains an N-terminal hemerythrin-like (Hr) domain that can directly bind iron (Chollangi et al., 2012; Salahudeen et al., 2009; Shu et al., 2012; Thompson et al., 2012; Vashisht et al., 2009). Topological changes of the FBXL5 Hr domain triggered by iron depletion have been shown to destabilize the F-box protein, thereby stabilizing IRP2. Structural studies of the FBXL5 Hr domain have revealed a di-iron center as the basis for iron sensing. However, the oxygen sensing mechanism of FBXL5 remains unresolved (Shu et al., 2012; Thompson et al., 2012). At the physiological level, loss of FBXL5 in mice leads to embryonic death, which can be rescued by co-deletion of IRP2 (Moroishi et al., 2011). The FBXL5-IRP2 axis, therefore, plays a central role in iron homeostasis *in vivo*.

Despite recent advances, FBXL5 research remains in its infancy with some fundamental questions poorly addressed. In particular, the mechanism by which the F-box protein specifically recognizes IRP2 has not been explored. Whether binding of IRP2 to FBXL5 is regulated by cellular signals, a phenomenon that has been frequently observed for other F-box protein-substrate interactions, remains an open question. In fact, emerging evidence hints at additional iron-sensing mechanisms that mediate FBXL5-IRP2 interaction independent of the FBXL5 Hr domain (Salahudeen et al., 2009; Thompson and Bruick, 2012; Vashisht et al., 2009). By means of integrated biochemical, biophysical, and structural analyses, we herein report the identification of a unique Fe-S cluster in FBXL5, which serves as a critical cofactor of the

ubiquitin ligase dictating the recruitment of IRP2 for its iron- and oxygen-dependent degradation.

Results

FBXL5 harbors a [2Fe2S] cluster

To probe IRP2 recognition by FBXL5, we set out to reconstitute their interactions with purified recombinant proteins. FBXL5 recruits IRP2 via a 492 amino acids region C-terminal to its Hr domain, which consists of an F-box motif and a leucine-rich repeat (LRR) domain (Salahudeen et al., 2009; Vashisht et al., 2009) (Figure S1A). Early studies have shown that IRP2 differs from IRP1 by a protease-sensitive 73 amino acids insertion, which is dispensable for FBXL5 binding (Dycke et al., 2007; Salahudeen et al., 2009; Vashisht et al., 2009). We accordingly constructed and purified the internally truncated IRP2 protein (IRP2Δ73) and FBXL5 lacking the Hr domain (FBXL5C492) together with the SCF adaptor SKP1. Despite being soluble, FBXL5C492-SKP1 was aggregation-prone and only weakly interacted with IRP2Δ73 (hereafter referred to as IRP2) (Figures 1A and 1B). Based on sequence analysis, we further optimized the F-box protein by deleting an LRR domain loop region that is less conserved and predicted to be structurally disordered (Figure S1B). In contrast to the original construct, this FBXL5 core fragment (FBXL5C492Δ) is not only mono-dispersed, but also highly competent in binding IRP2 (Figures 1A and 1B).

Unexpectedly, a concentrated sample of highly purified FBXL5C492Δ was brown in color (Figure 1C), suggesting the presence of an iron-containing prosthetic group. Its UV/vis absorption spectrum revealed peaks at 330 nm and 425 nm, as well as a broad shoulder at longer wavelengths (Figure 1C). These characteristics match the signature spectrum of a typical Fe-S cluster (Freibert et al., 2018). By contrast, IRP2 and purified aggregation-prone FBXL5C492 are clear and faintly colored, respectively, with few or less pronounced UV/vis absorption features (Figure 1C).

To identify the Fe-S cluster in FBXL5, we analyzed the FBXL5C492Δ sample using electron paramagnetic resonance (EPR). Both untreated and potassium ferricyanide oxidized samples were EPR silent and retained their brownish color, whereas sodium dithionite-reduced sample rapidly became pale-yellow and showed a prominent signal due to a spin-1/2 species with principal *g* values of 2.042(2), 1.918(5), and 1.889(5) and an average *g* value of 1.950(4) (Figure 1D). These *g*-values are consistent with a four-cysteine coordinated ferredoxin-type $[2Fe2S]^{+}$ cluster (Beinert et al., 1997; Liu et al., 2014; Shubin and Dikanov, 2006). Hence, isolated FBXL5 possesses a [2Fe2S] cluster in its oxidized $[2Fe2S]^{2+}$ state. Moreover, this FBXL5-bound [2Fe2S] cluster is redox-active as evidenced by its reduction by dithionite. To further validate the identity of the Fe-S cluster, we subjected the SKP1-complexed FBXL5C492Δ sample to native protein mass spectrometry analysis. The spectra of FBXL5C492Δ-SKP1 exhibited two distinct populations, representing the apo and the co-factor-bound forms. The mass difference between the two species is ~176 Da, which matches the molecular weight of a [2Fe2S] cluster (Figures 1E and S2). Collectively, we conclude that FBXL5 is a Fe-S protein containing a redox-active [2Fe2S] cluster.

Overall structure of IRP2-FBXL5-SKP1 complex

To elucidate the structural basis of FBXL5-IRP2 interaction and the role of the [2Fe2S] cluster, we assembled and determined the structure of an IRP2-FBXL5C492Δ-SKP1 complex bound to CUL1 N-terminal domain (NTD) at a resolution of 3.0 Å by single-particle cryo-electron microscopy (cryo-EM) (Figures 2 and S3; Table S1). With homology models of IRP2 and FBXL5C492Δ, the intermediate map obtained with unmasked 3D refinement readily unveiled the overall architecture of the quaternary complex (Figure 2A). Focused 3D refinement further

improved the quality of the map, which enabled us to manually rebuild the model of FBXL5C492Δ (hereafter referred to as FBXL5) and three of the four IRP2 domains (Figures 2B, 2C, and S4).

The IRP2-FBXL5-SKP1 complex adopts an overall structure reminiscent of a dragon, whose bulky head is formed by the multi-domain IRP2 protein with a winding neck represented by FBXL5-SKP1 (Figure 2D). IRP2 notably is in an L-shaped open conformation with its domain III and domain IV widely separated on two sides of the protein complex (Figures 2D and S5). IRP2 is recruited to the F-box protein predominantly through its domain IV. Like other F-box proteins, FBXL5 utilizes its three-helix F-box motif to engage the SCF adaptor protein SKP1 and folds its C-terminal LRR domain into a slender curved solenoid. Unlike most known LRR-containing F-box proteins, which recognize their substrates via either the concave or top surface of their LRR domains (Hao et al., 2005; Xing et al., 2013), FBXL5 captures IRP2 through the C-terminal end of its LRR domain. In close vicinity of the FBXL5-IRP2 interface is the striking [2Fe2S] cluster, which is cradled by a highly conserved and intertwined FBXL5 C-terminal loop (Figures 2D and S1).

Integrity of Fe-S cluster is essential for FBXL5 to recognize IRP2

The FBXL5 LRR domain is composed of six complete LRRs (LRR1–LRR6), which are capped by an additional β-strand preceding the C-terminal loop region (Figure 3A). The FBXL5 LRRs pack in tandem to form an arched assembly with a canonical β-strand-loop-α-helix structure in each repeating unit. Distinct from other β-strands in LRRs, the capping β-strand is led by two extra residues in sequence that form a horn at the basal ridge of the LRR fold (Figure S6). This feature is echoed at the apical ridge by the sequence succeeding the capping β-strand, which tilts

moderately and opens up a nest-like area. The subsequent FBXL5 loop packs against the α-helix of LRR6 and winds back to the nest area, creating a hook-like structure (Figure 3A). As discussed below, this structural element plays a vital role in docking IRP2 and, therefore, is named "interface loop". Following the "interface loop", the F-box protein terminates with a circled loop covering the nest area. We named it "lid loop" (Figure 3A).

A close examination of the nest area sequestered by the intertwining C-terminal fold reveals an extra rhombus-shaped density with a well-defined plane (Figures 3A and 3B). It is coordinated by four strictly conserved cysteine residues in the C-terminal loop region, including Cys662 following the capping β-strand, Cys676 in the "interface loop", and Cys686 and Cys687 in the "lid loop" (Figures 3B and 3C). In addition, a network of contacts surrounding the extra density helps maintain a generally hydrophobic environment of the site (Figure S7A). These features strongly suggest that the density belongs to the [2Fe2S] cluster identified in our biophysical studies. To validate this [2Fe2S] cluster coordination site, we purified four mutants of the F-box protein with each cysteine residue substituted by serine and a C-terminally truncated mutant lacking the last six C-terminal residues including the two consecutive cysteines (Cys686 and Cys687). As expected, the UV/vis absorption spectra of the C676S, C686S and C687S mutants displayed substantially diminished [2Fe2S] cluster peaks, while the C662S and tailless mutants lost all the spectral features of a Fe-S protein (Figure 3D). Together, our structural and mutational results unambiguously identify the location of the [2Fe2S] cluster-binding site and highlight the important role of the C-terminal loop region with the four ligand cysteine residues in stabilizing the cofactor.

While incorporation of the [2Fe2S] cluster is cooperatively mediated by the FBXL5 capping β-strand and C-terminal loop region, it is conceivable that the cluster cofactor would

reciprocally organize and stabilize the local structure of the C-terminal end of the FBXL5 LRR domain. Because of its physical proximity to the FBXL5-IRP2 interface, compromised integrity of the [2Fe2S] cluster is expected to directly impact the interaction between the ubiquitin ligase and its substrate. In consistence with this notion, all four cysteine missense mutations either pronouncedly weakened or largely abrogated the ability of FBXL5 to interact with IRP2 (Figure 3E). Similarly, the tailless F-box protein missing half of the "lid loop" lost its IRP2-binding activity. Incorporation of the [2Fe2S] cluster, therefore, is essential for FBXL5 to recognize IRP2 with an intact affinity.

Interface between FBXL5 and IRP2

Consistent with previous mutational analysis, IRP2 predominantly uses its domain IV to dock to the distal end of the FBXL5 LRR fold (Wang et al., 2008). The complementary FBXL5-IRP2 interface is surprisingly compact and is primarily mediated by loop structures from both sides (Figures 4A and 4B). The region in IRP2 domain IV responsible for binding FBXL5 is characterized by two spatially adjacent loops, Loop1 and Loop2, that are nucleated by four central hydrophobic residues, Ile761, Pro778, Phe781 and Tyr784 (Figures 4B and S8). Protruding out from Loop1 is a strictly conserved IRP2 residue, Arg779, which inserts its side chain deeply into the center of the FBXL5 "interface loop" (Figures 4B, 4D, and S8). In addition to a cation-π interaction with Tyr661 on the capping β-strand of FBXL5, IRP2 Arg779 is locked to the "interface loop" by donating hydrogen bonds to three backbone carbonyl groups of the F-box protein (Figure S7B). In Loop2, an auxiliary arginine residue, Arg763, stabilizes the peripheral interface by interacting with the negatively charged FBXL5 basal ridge horn and packing against Pro778 of Loop1 from IPR2 (Figures 4B and S7B). Together, Arg779 and

Arg763 coordinate to rivet IRP2 onto the lower portion of FBXL5 C-terminal loop region (Figure 4A). Meanwhile, the "lid loop" of FBXL5 is embraced by an α-helix ("arm helix") in domain I of IRP2, which forms a concave surface at the junction of IRP2 domain I and domain IV (Figures 4A, 4C, and S8). This engagement features a close packing between Arg224 of IRP2 and Arg688 of FBXL5, both of which are neutralized by the surrounding residues via a cluster of polar interactions (Figures 4C, S1, and S8).

Although the [2Fe2S] cluster of FBXL5 is not situated at the immediate FBXL5-IRP2 interface, it contributes to IRP2 recognition by securing several critical interactions. First, the backbone carbonyls of two cluster ligand cysteines, Cys662 and Cys676, are tied to IRP2 by hydrogen bonding with Arg779 and Ser760, respectively (Figure 4D). Second, Leu679 of FBXL5, which guards the nonpolar environment of the cluster, directly packs against IRP2 Loop1 (Figure 4D). This local intermolecular contact is further strengthened by its nearby FBXL5 residue, Gln680, whose side chain forms a hydrogen bond with IRP2 Gly759. Above all, the central role of the [2Fe2S] cluster in shaping the complementary surface of FBXL5 manifests its indispensability in IRP2 recruitment.

To map the key structural elements supporting FBXL5-IRP2 interaction, we tested a series of FBXL5 and IRP2 mutants based on our structural analysis. Substitution of IRP2 Arg763 modestly affected complex formation (Figure 4E), indicating an accessary role of the residue at the interface. By contrast, FBXL5 binding was completely abolished by substitution of IRP2 Arg779 (R779E), which represents a "hot spot" for FBXL5 association (Figure 4E). Correspondingly, alteration of FBXL5 Tyr661 (Y661R) that directly contacts IRP2 Arg779 markedly compromised IRP2 recognition (Figure 4E). Interestingly, none of the remaining single amino acid substitution mutants showed detrimental effect on the FBXL5-IRP2 interaction,

suggesting that the FBXL5-IRP2 interface is multivalent and distributive. Indeed, a combination of mutations introduced at more than one region of the interface severely impaired IRP2 association, as exemplified by the FBXL5 L679R/D663R double mutants (Figure 4E).

Previously studies have shown that, distinct from the wild-type protein, an IRP1 mutant defective in binding [4Fe4S] cluster can be recognized by FBXL5 and undergo proteasomal degradation (Salahudeen et al., 2009; Vashisht et al., 2009). In light of our structure, this can be rationalized by all the key residues at the FBXL5-IRP2 interface, which are also conserved in IRP1, and the open conformation of apo-IRP1 (Walden et al., 2006) (Figures S5 and S8). A structural comparison between the holo-IRP1 protein (Dupuy et al., 2006) and an FBXL5-IRP1 model generated from our structure indicates that FBXL5 would clash with IRP1 domain III, which has been shown to rotate towards domain IV upon [4Fe4S] cluster insertion (Figure 4F). By incorporating the cluster cofactor, IRP1 effectively shields its potential interface for FBXL5 binding. Our structure of the FBXL5-IRP2 complex, therefore, provides a structural explanation for the mechanism by which cellular holo-IRP1 is spared from FBXL5-mediated degradation.

Ability of FBXL5 to dislodge IRP2 from IRE

The IRP proteins have been previously shown to bind IREs with high affinities. How IRP2 is effectively decoupled from IREs and degraded has been poorly understood. The overall resemblance of IRPs in the FBXL5-IRP2 and IRE-IRP1 structures allowed us to derive a model of the IRP2-IRE complex. A side-by-side comparison of IRP2 in the FXBL5- and IRE-complexed forms readily reveals that IRP2 domain IV is equally exploited by the two binding partners (Figure 5A). Specifically, the last three LRRs and the C-terminal loop region of FBXL5 occupy the same space next to IRP2 domain IV as the helical region of IRE does. Their shared

binding modes, thus, preclude IRP2 from simultaneous engagement with the ubiquitin ligase and the RNA element. Moreover, FBXL5 and IRE have developed their distinctive means to further immobilize the multi-domain IRP2 protein. The "lid loop" of the F-box protein hooks the "arm helix" of IRP2 domain I, whereas the terminal loop of IRE specifically clinches IRP2 domain III (Figure 5A). These interactions fix IPR2 in a similar L-shaped open conformation in both structures. Altogether, these structural comparisons raise the possibility that FBXL5 might be able to directly compete with IRE for IRP2 binding.

To test this idea, we developed an Amplified Luminescence Proximity Homogeneous Assay (AlphaScreen) to quantitatively assess the ability of FBXL5 to displace IRE from IRP2 *in vitro*. Biotinylated IRE and GST-fused IRP2 were immobilized on the donor and acceptor beads, respectively, which yielded a robust luminescence signal due to stable complex formation. By titrating the concentration of label-free IRP2 and FBXL5, we were able to obtain dose-response curves and the half maximal inhibitory concentration (IC_{50}) for the competitors. Remarkably, IRP2 abolished the luminescent signal with an IC_{50} of 0.35 nM, while FBXL5 achieved the same effect with an IC_{50} of 0.12 nM (Figure 5B). Therefore, FBXL5 is equally, if not more, potent than IRP2 in disrupting an existing IRE-IRP2 complex. Overall, these results suggest that the FBXL5-IRP2 and IRE-IRP2 complexes are comparable in affinity and the F-box protein is capable of physically dislodging IRP2 from IRE.

Oxygen-dependent FBXL5-IRP2 interaction

The critical role of the FBXL5 [2Fe2S] cluster in binding IRP2 and its redox active property prompted us to next investigate whether changes in the redox state of the cluster affect the association between the two proteins. To reduce the [2Fe2S] cluster, we pretreated FBXL5

samples with sodium dithionite at increasing concentrations and monitored their binding to IRP2 (Figure 5C). In a dose-dependent manner, dithionite was able to reduce the cluster to its $[2Fe2S]^{+}$ state and compromise the ability of FBXL5 to interact with IRP2 (Figures 1D and 5D, lane 3–6). To prevent FBXL5-bound [2Fe2S] cluster from being rapidly re-oxidized by oxygen in the ambient air, we repeated the assay under the anaerobic condition. Surprisingly, untreated FBXL5 retained the ability to bind IRP2, whereas FBXL5 treated with 2 mM dithionite essentially lost its IRP2-binding activity (Figures 5C and 5D, lane 7, 8). Notably, the same concentration of dithionite only weakened but not abolished the interaction under aerobic condition (Figure 5D, lane 3, 4). To rule out the possibility that the [2Fe2S] cluster was permanently damaged during anaerobic reduction, we monitored the dithionite-treated and subsequently re-oxidized sample by UV/vis spectrum. In contrast to the less featured spectrum of FBXL5 in its reduced state, the re-oxidized sample regained the characteristic peaks, indicating that both oxidation and reduction of the [2Fe2S] cluster are reversible (Figure 5E). Remarkably, after we transferred the anaerobically reduced FBXL5 sample, which was deficient for IRP2 binding and had passed through the column with immobilized IRP2, back to aerobic condition, the interaction between FBXL5 and IRP2 was largely restored (Figures 5C and 5D, lane 9). Altogether, these experiments establish FBXL5-bound [2Fe2S] cluster as a reversible redox switch, which confers oxygen-dependence for IRP2 binding.

Discussion

In this study, we uncover a [2Fe2S] cluster as an FBXL5 cofactor, which plays a critical role in controlling the recruitment and polyubiquitination of IRP2 in iron homeostasis. In conjugation with the previous reports of iron binding to the N-terminal Hr domain of the F-box protein, our findings unveil a plausible two-tiered mechanism by which FBXL5 senses the levels of iron to dictate IRP2 stability (Figures 6 and S9). Although the relative abundance of labile iron and [2Fe2S] cluster remains to be determined, it is generally thought that the cellular concentration of labile iron is kept at a minimal level due to its toxicity. It is conceivable that the two sensor domains of FBXL5, namely the N-terminal Hr domain and the C-terminal LRR domain, perceive iron at two different levels. While the Hr domain governs the stability of the ubiquitin ligase upon iron depletion, the LRR domain with its iron-sulfur cluster might determine IRP2 turnover rate in response to increasing iron levels as reflected by the availability of the [2Fe2S] cluster. The importance of the FBXL5-bound [2Fe2S] cluster in IRP2 regulation is manifested by the pronounced accumulation of IRP2 coincided with the impaired Fe-S cluster biogenesis (Tong and Rouault, 2006; Ye et al., 2010).

Besides coupling IRP2-FBXL5 interaction with iron availability, our biochemical studies suggest that the [2Fe2S] cluster cofactor of FBXL5 is capable of linking IRP2 binding to oxygen, which has an intricate relationship with iron. By monitoring FBXL5-IRP2 interaction with highly purified recombinant proteins, we demonstrate that the [2Fe2S] cluster is reversibly redox active and only supports IRP2 binding to FBXL5 when it is oxidized by oxygen to the $[2Fe2S]^{2+}$ state. This special property might allow the iron-sulfur cluster to fine-tune FBXL5-IRP2 complex formation, thereby tailoring IRP2 degradation based on the oxygen level in different tissues and under various physiological conditions. The molecular basis for the redox-dependent

FBXL5-IRP2 interaction might reside in the unique coordination of the [2Fe2S] cluster in FBXL5 by two adjacent cysteines. Upon reduction, the geometry of these cysteines and their nearby residues might be conformationally re-arranged, a phenomenon that has been described for the N2 Fe-S cluster from respiratory complex I (Berrisford and Sazanov, 2009). Such structural changes could lead to re-organization of the FBXL5 C-terminal loop region, which blocks IRP2 binding. Further studies of FBXL5 with its [2Fe2S] cluster in the reduced state will shed light on the underlying structural mechanism.

Recent studies have revealed an interaction between FBXL5 and the cytosolic iron-sulfur cluster assembly (CIA)-targeting complex, which is sensitive to oxygen and promotes IRP2 ubiquitination (Mayank et al., 2019; Tan et al., 2013). While it is tempting to speculate that the [2Fe2S] cluster is loaded onto FBXL5 by the CIA-targeting complex, their functional relationship calls for further investigation. In contrast to the four [2Fe2S]-coordinating cysteines, the FBXL5 sequence responsible for binding the CIA-targeting-complex is only conserved in mammalian FBXL5 orthologs. Moreover, abrogation of FBXL5-CIA interaction only partially compromised IRP2 binding to the F-box protein, which is inconsistent with an essential role in delivering the [2Fe2S] cluster to the E3 ligase. It remains possible that the FBXL5-CIA-targeting complex interaction might have evolved as a separate and redundant mechanism for regulating FBXL5-mediated IRP2 degradation.

Substrate recognition by ubiquitin E3 ligases is susceptible to regulation by a variety of cellular signals (Ravid and Hochstrasser, 2008; Zheng and Shabek, 2017). FBXL5 represents the first example of a human ubiquitin ligase that sports an ancient protein co-factor, which usually mediates oxidation-reduction catalytic reactions, but is repurposed by evolution to control oxygen-responsive protein-protein interactions, and, indirectly, RNA-protein interactions. Our

discovery not only underscores the functional versatility of ubiquitin ligases as signaling hubs, but also the multifaceted role of iron-sulfur clusters in biology.

Acknowledgments

We thank the cryo-EM facility at the University of Washington and J. D. Quispe for technical support in electron microscopy data acquisition, J. Kollman and M. C. Johnson at University of Washington, W. Huang at Case Western Reserve University for help in data processing, P. Cresswell in Yale for the gift of *suf* operon plasmid, J. A. Leigh and L. Gu at the University of Washington for the access to the anaerobic glove boxes in their labs, T. R. Hinds for help on data analysis of AlphaScreen assay, and the members of Zheng lab for help. This work was supported by funds from the Howard Hughes Medical Institute (N.Z.), National Science Foundation (CHE-1807382 to M.F.B.), and National Institutes of Health (T32GM008268 to E.R.C., R01DK107712 to E.A.L.).

Author Contributions

H.W. and N.Z. conceived the project. H.W. constructed and purified all protein samples in this study and performed the protein binding, UV/vis and AlphaScreen assays. Both H.W. and H.S. performed grid preparation and optimization. H.S. carried out electron microscopy data collection, processing and reconstruction. H.W. and N.Z. built the atomic model and analyzed the structure. E.R.C. and S.S. designed and conducted EPR experiments. S.H. and M.F.B. designed and conducted native mass spectrometry experiments. H.W. and N.Z. wrote the manuscript with input from E.A.L. and other authors.

Declaration of Interests

N.Z. is a member of the scientific advisory board of Kymera Therapeutics and a co-founder of Coho Therapeutics.

Figure Legends

Figure 1. FBXL5 possesses a [2Fe2S] cluster

(A) Size-exclusion chromatography analysis of two FBXL5 constructs bound to SKP1. Elution profiles of the aggregation-prone FBXL5C492 and mono-dispersed FBXL5C492Δ samples are shown in gray and blue, respectively.

(B) GST pull-down assay using recombinant GST-IRP2Δ73 and purified FBXL5C492 and FBXL5C492Δ with GST as a negative control. The black arrow indicates a specific band of FBXL5C492 in small amount.

(C) Colors and UV/vis absorption spectra (300-750 nm range) of the purified FBXL5C492, FBXL5C492Δ, and IRP2 protein samples. All protein samples recorded for UV spectra and color display are at the concentration of 8.0 mg/mL.

(D) 9.425 GHz EPR spectra of FBXL5C492Δ in oxidized, reduced and as-isolated states. Simulation (red) parameters: g values 2.042, 1.918, and 1.889, g-strain widths 0.0001, 0.0006, and 0.0006; 1 mT Lorentzian FWHM line broadening. The asterisk indicates an organic radical.

(E) Native mass spectrometry analysis of the FBXL5C492Δ-SKP1 complex. The region assigned to the 13+ ions exhibits two features corresponding to the apo and the [2Fe2S] cluster-containing complexes. The top axis shows the mass relative to the apo complex.

See also Figures S1 and S2.

Figure 2. Cryo-EM structure of the IRP2-FBXL5-SKP1 complex

(A) A 3.9 Å electron microscopy map fit with structural models of IRP2 (wheat), FBXL5 (teal), SKP1 (green) and CUL1NTD (gray).

(B) 3D reconstruction of the IRP2-FBXL5-SKP1-CUL1NTD complex at an overall resolution of 3.0 Å is colored according to local resolution estimated by ResMap.

(C) The structure of the IRP2-FBXL5-SKP1 complex modeled with the 3.0 Å density map shown in (B).

(D) Two orthogonal views of the IRP2-FBXL5-SKP1 complex shown in ribbon diagram with the same color scheme as shown in (A). The [2Fe2S] cluster is shown in spheres. The N and C termini of different proteins are labeled N and C in corresponding colors.

See also Figures S1, S3, S4, and S5; Table S1.

Figure 3. Integrity of the [2Fe2S] cluster is essential for the FBXL5-IRP2 interaction

(A) Ribbon diagram of the LRR domain of FBXL5 (teal) containing the [2Fe2S] cluster (spheres). The capping β-strand (slate), interface loop (magenta) and lid loop (brown) are labeled and colored. Select LRRs are numbered and labeled.

(B) A close-up view of the [2Fe2S] cluster (spheres) ligated by four cysteines (sticks) from the capping β-strand (slate), interface loop (magenta) and lid loop (brown). A density map at 3.0 Å resolution covering the [2Fe2S] cluster and its cysteine ligands is shown in gray mesh at contour level of 2.0 σ. For clarity, the residues in the utmost C-terminus of FBXL5 are not shown.

(C) Sequence alignment of the C-terminal loop region in FBXL5 orthologs from human (*Homo sapiens*), mouse (*Mus musculus*), bird (*Taeniopygia guttata*), frog (*Xenopus tropicalis*), fish (*Danio rerio*), lancelet (*Branchiostoma belcheri*), insect (*Zootermopsis nevadensis*), and seashell (*Oyster*). Strictly conserved residues are colored black with key structural elements at the C-terminal loop region labeled. Cysteines as [2Fe2S] cluster ligands are highlighted in yellow.

(D) UV/vis absorption spectra (300-750 nm) of FBXL5 WT and mutants measured at a protein concentration of 15.0 mg/mL.

(E) Analysis of IRP2-FBXL5 interaction by GST pull-down assay using recombinant GST-IRP2 and FBXL5 WT and mutants.

See also Figures S6 and S7.

Figure 4. Interface between FBXL5 and IRP2

(A) An overall view of the interface formed by FBXL5-LRRs (teal ribbons) containing the [2Fe2S] cluster (spheres) and IRP2 (wheat surface). For clarity, domain III of IRP2 is not shown.

(B-D) Close-up views of FBXL5-IRP2 interface around Loop1/2 of IRP2, Interface loop of FBXL5, Arm helix of IRP2, and the [2Fe2S] cluster. FBXL5 is shown in teal ribbon or surface, while IRP2 is shown in wheat ribbon or surface. The [2Fe2S] cluster is shown in spheres. Select interface residues are shown in sticks. Dashed lines in brown represent hydrogen bonds and polar interactions. The C terminus of FBXL5 is labeled C in teal or black.

(E) GST pull-down assay assessing the ability of FBXL5 WT and mutants to bind IRP2.

(F) Comparison of IRP1 structures in the FBXL5-IRP1 model and the [4Fe4S] cluster bound holo-aconitase (PDB: 2B3X). FBXL5-LRRs is shown in ribbon, while IRP1 is shown in surface with domain I/II in yellow, domain III in orange, and domain IV in wheat. The [2Fe2S] and [4Fe4S] clusters are shown in spheres. The orange arrow indicates the movement of IRP1 domain III for incorporating the [4Fe4S] cluster.

See also Figures S1, S5, S7, and S8.

Figure 5. Functional analysis of FBXL5-IRP2 interaction

(A) Structural comparison of IRP2-FBXL5 complex and the modeled IRP2-IRE complex. FBXL5 (teal) and Ferritin H IRE (slate) are shown in ribbon, while IRP2 is shown in surface with domain I/II in yellow, domain III in orange, and domain IV in wheat. The [2Fe2S] cluster is shown in spheres. The IRP2-IRE model is generated on the basis of the known structure of the IRP1-Ferritin H IRE complex (PDB: 3SNP). Critical IRP2-contacting elements of FBXL5 and IRE are labeled correspondingly.

(B) AlphaScreen assay assessing the ability of FBXL5 to compete with Ferritin H IRE for binding IRP2. Data were measured in triplicate and plotted as mean ± SD.

(C) A schematic diagram showing the GST pull-down assays for assessing the IRP2-binding abilities of untreated and sodium dithionite-treated FBXL5 with [2Fe2S] cluster in different redox states under aerobic or anaerobic conditions.

(D) Experimental results of (C) as analyzed by SDS-PAGE.

(E) UV/vis spectra (300-750 nm) of the FBXL5 samples tested in (C) and (D) at the same concentration.

Figure 6. A model for the FBXL5-IRP2 axis regulation by iron and oxygen

In iron-depleted cells, the N-terminal Hr domain of FBXL5 cannot bind iron and undergoes conformational changes that destabilizes the entire protein. When iron is present at low levels, FBXL5 is stabilized. Increasing levels of iron facilitate the production of [2Fe2S] cluster, which is incorporated into the C-terminal LRR domain of FBXL5. Only when oxygen level is high enough to maintain the cluster in its oxidized $[2Fe2S]^{2+}$ state could the SCF^{FBXL5} E3 ligase recruits IRP2 as a substrate for polyubiquination and degradation. The physical interaction

between IRP2 and FBXL5 might help release IRP2 from IREs to alter the translation of iron metabolism genes.

See also Figure S9.

Methods

Protein expression and purification

The human IRP2 protein was expressed as a glutathione S-transferase (GST) N-terminal fusion protein in HighFive monolayer insect cells and isolated by glutathione affinity and subsequent anion exchange chromatography after off-column cleavage by tobacco etch virus (TEV) protease. The human FBXL5 and SKP1 proteins were co-expressed and produced in BL21 (DE3) *E.coli* cells in media supplemented with cysteine and Ferric ammonium citrate (FAC) at the concentrations of 121 mg/L and 25 mg/L, respectively. The plasmid encoding operon *suf* was co-transformed when needed. The FBXL5-SKP1 complex was purified by nickel affinity and subsequent anion exchange chromatography after off-column cleavage by TEV protease. Human CUL1NTD was expressed as a glutathione S-transferase (GST) N-terminal fusion protein in BL21 (DE3) *E.coli* cells and purified similarly to IRP2. To assemble the complex of IRP2-FBXL5-SKP1-CUL1NTD for cryo-EM study, the individually isolated proteins were mixed in stoichiometric amounts and subsequently applied to the Superdex-200 gel filtration column (GE Healthcare) in a buffer containing 20 mM Tris-HCl, pH 8.0, 150 mM NaCl and 5 mM DTT (dithiothreitol). The mono-dispersive peak in the elution profile contained the tetrameric complex with a mass of ~200 kDa. All the purification procedures were performed at 4°C. The mutants of FBXL5 and IRP2 were expressed and isolated in the same way as the WT proteins. The affinity tag may be left on the proteins for the purposes of different assays.

Cryo-EM sample preparation and data collection

To prepare grids for cryo-EM data collection, an UltraAuFoil R1.2/1.3 grid (Quantifoil Micro Tools GmbH) was glow discharged for 2 minutes at 20 mA with a glow discharge cleaning

system (PELCO easiGlow). 3.0 μL of the purified IRP2-FBXL5-SKP1-CUL1NTD complex at 0.5 mg/mL was applied to a freshly glow-discharged grid. After incubating in the chamber at 4 °C and 100% relative humidity, grids were blotted for 4 s with a blotting force of zero, then immediately plunge-frozen in liquid ethane using a Vitrobot Mark IV system (Thermo Fisher Scientific). Data collection was carried out on a Titan Krios transmission electron microscope (Thermo Fisher Scientific) operated at 300 kV. Automation scheme was implemented using the Leginon software (Suloway et al., 2005) at a nominal magnification of 130 K, resulting a physical pixel size of 1.056 Å. Zero-loss-energy images were acquired on a Gatan K2 Summit direct detector operated in super-resolution counting mode (pixel size in super-resolution mode is 0.528 Å), with the slit width of post-column Gatan Quantum GIF energy filter set to be 20 eV. The dose rate was adjusted to 8.2 electrons per $Å^2$ per second, and a total dose of 73.8 electrons per $Å^2$ for each image were fractionated into 60 frames. Data were collected in four sessions with a defocus range of 1.5-3 μm. In total, 5,768 movies were collected with CompuStage in the microscope non-tilted, and a set of 1172 movies were acquired when the CompuStage was tilted 40 degrees.

Image processing and 3D reconstruction

Alignment of movie frames was performed using MotionCor2 (Zheng et al., 2017) through the RELION3.0 pipeline (Kimanius et al., 2016) with images binned 2 in both dimensions by Fourier cropping, resulting in a pixel size of 1.056 Å of the summed images. Dose-weighted summed images were imported into cisTEM (Grant et al., 2018) for manual inspection to remove bad images. The final set of good images contained 5,309 non-tilted and 475 40-degree-tilted images. Around 114,000 particles were selected automatically on a subset of both non-tilted and

tilted images after estimation of contrast transfer function using CTFFIND4 (Rohou and Grigorieff, 2015) within cisTEM (Grant et al., 2018) and were subjected to 2D classification to generate 2D averages, which were used later as templates for automatic particle picking. Later steps of data processing were all implemented within the RELION3.0 pipeline (Kimanius et al., 2016). The parameters of contrast transfer function were estimated using cleaned non-dose-weighted motion-corrected sums by GCTF (Zhang, 2016). Template-based automatic particle picking resulted in a set of 2,832,595 particles. GCTF (Zhang, 2016) was used again to perform per-particle estimation of the parameters of contrast transfer function on the automatically picked particles. Particles were then extracted from dose-weighted motion-corrected sums and 3X binned to a box size of 108 pixels. After 3 rounds of reference-free 2D classification, a total of 1,716,405 particles were selected from the original pool. A 3D density map was obtained by employing the 3D initial model job-type within RELION3.0 from a subset of 2D-cleaned-up particles, which was low-pass-filtered to 60 Å and was used as the initial model for 3D classification. A pool of 955,060 particles belonging to the best class from 3D classification were selected, extracted without binning, and subjected to 3D auto-refine without applying a mask, which gave rise to a reconstruction of 3.9 Å. The post-processing procedure with a soft mask generated in RELION3.0 reported an estimated resolution of 3.2 Å. To improve the resolution, CTF refinement (Zivanov et al., 2018) was executed to refine the defocus values for each particle and to calculate the beam-tilt parameters for each separate data-collection session. The resulting particles were polished through the Bayesian polishing approach in RELION3.0 (Zivanov et al., 2019). These polished shiny particles went through another round of focused 3D refinement by imposing a soft mask surrounding the region of interest, which comprises most of mass of the complex, including SKP1, FBXL5, and domains I, II and IV of IRP2. The final reconstruction

was measured to be at a resolution of 3.0 Å, and the map was post-processed in RELION3.0, with correction for the modulation transfer function and sharpened by applying a global B-factor of -78 $Å^2$ that was estimated in the post-process protocol. Reported resolutions are based on the gold-standard FSC (Fourier shell correlation) using the 0.143 criterion (Rosenthal and Henderson, 2003). ResMap (Kucukelbir et al., 2014) was used to determine local resolution.

Model building and refinement

Initial model building was performed on the basis of the resulting map at 3.0 Å after local refinement using a mask to exclude the less-defined flexible regions. Considering that the crystal structures of IRP1 were determined in two different conformations (as an aconitase with PDB ID: 2B3X and as an IRE-binding protein with PDB ID: 3SNP, 3SN2), we used the structures of individual domains in IRP1 as the templates to build the model of IRP2. Models of four domains of IRP1 were fitted into the map as rigid bodies in Chimera (Pettersen et al., 2004) with domain I, II, IV well docked and domain III unassigned due to the lack of density. All the amino acids were changed to the sequence of IRP2 and the model was manually rebuilt in COOT (Emsley et al., 2010). The model of FBXL5 was built *de novo* in COOT based on the map showing clear side chain densities of the residues in majority, while the crystal structure of SKP1 in GGTase3-FBXL2-SKP1 complex (PDB ID: 6O60) was used as the template for the model building of SKP1. Iterative rounds of real-space refinement in PHENIX (Adams et al., 2010) and manual adjustment in COOT were carried out for model improvement. The final model was evaluated using MolProbity and the cryo-EM data collection, refinement and validation statistics are summarized in Table S1.

Affinity pull-down assay

The GST pull-down assay was performed using ~500 μg of purified GST or GST-tagged IRP2 WT or mutant proteins as the bait and ~400 μg of His-tagged FBXL5 WT and mutant proteins. Reaction mixtures were incubated with 100 μL GST beads (GE Healthcare) at 4°C for 1 hour in the binding buffer with 20 mM Tris-HCl, pH 8.0, 150 mM NaCl and 5 mM DTT. After extensive wash with binding buffer, the protein complexes on the beads were eluted by 5 mM glutathione. The eluted samples were resolved by SDS-PAGE and analyzed by Coomassie staining. For the pull-down assays with reduced FBXL5, the purified His-tagged FBXL5 WT proteins were treated with 2 mM, 4 mM and 8 mM DT (sodium dithionite) in ambient air or 2 mM DT in an anaerobic glove box (McCoy), and immediately applied to the binding reaction following the same protocol described above. The IRP2-binding-deficient FBXL5 FT (flow through) sample was re-oxidized overnight in ambient air and reapplied to the binding reaction next day (Figure 5C). Inputs represent 3–5% of the total amount of proteins used for each reaction.

UV/vis absorption spectrometry

UV/vis absorption spectra were recorded with 1 μL of protein samples under aerobic conditions at RT on a NanoDrop 2000c Spectrophotometer (Thermo Fisher Scientific) in a range from 220 to 750 nm. The protein samples were at the concentrations of 8.0 mg/mL or 15.0 mg/mL in the buffer containing 20 mM Tris pH 8.0, 150 mM NaCl and 5 mM DTT. The reduced sample of FBXL5 was prepared anaerobically prior to the aerobic UV/vis spectrum and subsequently re-oxidized overnight in the ambient air. The UV/vis spectrum of the re-oxidized sample was recorded next day.

EPR

The EPR samples were prepared from 300 μM FBXL5C492Δ-SKP1 protein complex in 20 mM Tris pH 8.0, 150 mM NaCl, 5 mM DTT and 20% (v/v) Glycerol. The reduced EPR sample was prepared in an anaerobic box (McCoy) by the addition of 1.5 mM freshly prepared DT (sodium dithionite). The oxidized sample was prepared aerobically by the addition of 1 mM $K_3Fe(CN)_6$. About 100 μL of solutions were transferred to 4 mm O.D. quartz tubes (Wilmad) and flash-frozen in liquid nitrogen. Atmosphere was removed by freeze-pump-thawing and the samples were flame sealed. X-band EPR spectra were collected on a Bruker EMX spectrometer equipped with an SHQE resonator. The sample temperature was set to 20 K utilizing an Oxford ESR900 liquid-helium flow cryostat. The modulation amplitude was 15 G, microwave power was 32 mW, and the sweep rate was 4 mT s^{-1}. The magnetic-field axis was calibrated with a teslameter, and the frequency was measured using a frequency counter. The spectrum was simulated using EasySpin (Stoll and Schweiger, 2006).

Native Mass Spectrometry

FBXL5C492Δ-SKP1 protein complex was buffer exchanged into aqueous 200 mM ammonium acetate at pH 7.0 using centrifugal concentrators (10 kDa MWCO, Spin-X UF, Corning, Inc.) and a centrifuge operated at 4°C. The protein sample used in positive ion mode was also heated using a heating block at ~52°C for one minute prior to analysis. The protein sample was loaded into glass capillaries with inner diameters of 0.78 mm that were pulled to approximately 1 to 3 μm on one end using a micropipette puller (P-97, Sutter Instruments, Novato, CA) for nano electrospray ionization. 10 μM of sample was loaded onto the glass capillary. Electrical contact with the solution was attained by inserting a platinum wire electrode into the wide end of the

capillary (Davidson et al., 2017). To minimize impurity carryover between experiments, the electrode was washed with aqueous 25% HCl (v:v) and rinsed with ultrapure (18.2 MΩ) water between samples. Data were acquired using a Waters Synapt G2 HDMS hybrid mass spectrometer (Giles et al., 2011) (Waters Co., Wilmslow, UK) in which the traveling-wave ion mobility cell was replaced with a radio-frequency (RF) confining drift cell (Allen et al., 2016) that contained approximately 1.7 Torr He. The following MS parameters were used for positive ion mode spectrum: capillary voltage, less than 1.0 kV; sampling cone, 70 V; extraction cone, 5 V; source temperature, ~30°C; trap collision energy, 50 V. The following MS parameters were used for negative ion mode spectrum: source temperature, ~30°C; extraction cone, 2 V; trap collision energy, 30 V; sampling cone: 50 V; trap gas flow: 1 ml/min. Mass spectra were analyzed using MassLynx v4.1 (Waters, Co., Milford, MA).

AlphaScreen Luminescence Proximity Assay

AlphaScreen assays for determining and measuring protein-protein and protein-RNA interactions were performed using EnSpire reader (PerkinElmer). Biotinylated Ferritin H IRE (pre-treated as described below) was immobilized to streptavidin-coated AlphaScreen donor beads. GST-tagged IRP2 was attached to anti-GST AlphaScreen acceptor beads. The donor and acceptor beads were brought into proximity by the interaction between IRE and IRP2. When excited by a laser beam of 680 nm, the donor beads emit singlet oxygen that activates thioxene derivatives in the acceptor beads, which then release photons of 520–620 nm as the binding signal. Competition assays were performed by titrating the concentrations of the tag-free IRP2 and FBXL5 as competitors in the pre-mixed IRE-IRP2 complex and measuring the half maximal inhibitory concentration (IC_{50}) for competitors based on the dose response curves showing signal recession.

The experiments were conducted in triplicates with 0.15 nM biotinylated Ferritin H IRE RNA and 0.15 nM GST-IRP2 in the presence of 5 μg/ml donor and acceptor beads in a buffer of 25mM Hepes pH 7.7, 150 mM NaCl, 5 mM DTT and 0.1% BSA. The concentrations of IRP2 and FBXL5 as competitors ranged from 0.02 nM to 150 nM. IC_{50} values were determined using non-linear curve fitting of the dose response curves generated with Prism 8 (GraphPad).

The biotinylated Ferritin H IRE RNA was synthesized from Integrated DNA Technologies (IDT). The lyophilized RNA was dissolved in RNase-free water and diluted to 200 μM in concentration. This stock solution was heated at 95°C for 5 min and then cooled in an ice bath for 10 min before being aliquoted. All the aliquots were stored at -80°C to avoid degradation and directly applied to assays after thawing.

Contact for Reagent and Resource Sharing

Further information and requests for resources and reagents should be directed to and will be fulfilled by the Lead Contact, Ning Zheng (nzheng@uw.edu).

Experimental Model and Subject Details

For DNA extraction, *E.coli* DH5α was used. For bacmid production, *E.coli* DH10Bac was used. For baculovirus production and amplification, Sf9 insect cells were used. For protein expression, both *E.coli* BL21(DE3) and HighFive insect cells were used.

Quantification and Statistical Analysis

Protein quantification was done using the Bradford Protein Assay protocol and Bio-rad Protein Assay Dye on a NanoDrop 2000c Spectrophotometer (Thermo Fisher Scientific) at RT.

Data and Software Availability

Cryo-EM density map of the IRP2-FBXL5-SKP1 complex has been deposited in the Electron Microscopy Data Bank (EMDB) under the accession code EMDB: XXX. Atomic coordinates have been deposited to the Protein Data Bank (PDB) with the accession number PDB: XXX.

Supplemental Figure Legends

Figure S1. FBXL5 and IRP2 domain organization and sequence alignment of FBXL5, Related to Figures 1, 2, and 4

(A) Domain organization and construct design of human FBXL5 and IRP2. Hr refers to hemerythrin-like.

(B) Alignment and secondary structure assignments of FBXL5 without Hr domain are generated by using sequences of selected orthologs from human (*Homo sapiens*), mouse (*Mus musculus*), bird (*Taeniopygia guttata*), frog (*Xenopus tropicalis*), fish (*Danio rerio*), lancelet (*Branchiostoma belcheri*), and seashell (*Oyster*). Secondary structure elements including α-helices and β-strands are indicated as cylinders and arrows, respectively. Dashed lines represent regions of the protein that are disordered in the solved structure. The internal deleted region is shadowed in gray, and the F-box motif helices are labeled green. Strictly conserved residues are colored black. The key structural elements at the C-terminal loop region are colored and labeled correspondingly. Cysteines as [2Fe2S] cluster ligands are highlighted in yellow. Green arrows at bottom indicate critical IRP2-binding residues, while black dots on top indicate the [2Fe2S] cluster stabilizing residues.

Figure S2. Native mass spectrometry analysis of the FBXL5C492Δ-SKP1 complex, Related to Figure 1

Native mass spectra of the FBXL5C492Δ-SKP1 complex acquired in positive and negative ion mode are shown in (A) and (B), respectively. These spectra each exhibit two predominant series of peaks. The lower-intensity series corresponds in mass to the apo-FBXL5C492Δ-SKP1 complex. The high-intensity series corresponds in mass to the [2Fe2S] cluster bound

FBXL5C492Δ-SKP1 complex. The enlarged spectra for 13+ and 13− ions are shown in (C) and (D) respectively. The qualities of the spectra acquired in negative ion mode are poorer. However, they are consistent with the assignments made for spectrum acquired in positive ion mode.

Figure S3. Cryo-EM analysis of the IRP2-FBXL5-SKP1-CUL1NTD complex by single-particle reconstruction, Related to Figure 2

(A) SDS-PAGE analysis of the purified IRP2-FBXL5-SKP1-CUL1NTD complex with all four components in equal stoichiometry.

(B) A representative cryo-EM image (non-tilted) of the IRP2-FBXL5-SKP1-CUL1NTD complex shows good particle distribution. Scale bar, 50 nm.

(C) 2D averages of the cryo-EM dataset, revealing features of secondary structure. Scale bar, 10 nm.

(D) Flowchart of single particle analysis for the IRP2-FBXL5-SKP1-CUL1NTD complex.

(E) The angular distribution of the particles included in the final reconstruction, with the side view of the density map of the complex shown in yellow.

(F) Gold standard (black) and model/map (pink) Fourier shell correlation curves for the final reconstruction.

Figure S4. Gallery of representative density for the IRP2-FBXL5-SKP1 complex, Related to Figure 2

Representative density in gray mesh from the 3.0 Å resolution electron microscopy map is shown for loop1, loop2, and arm helix regions of IRP2 (model in wheat); and interface loop, lid

loop, capping β-strand, LRR6, LRR4, and LRR2 regions of FBXL5 (model in teal). The density maps are displayed in PyMOL at contour level of 1.5-2.0 σ.

Figure S5. IRP2 adopts an L-shaped open conformation, Related to Figures 2 and 4

(A) Side view of IRP2 recognized by FBXL5 in surface representation.

(B) IRP1 in IRP1-Ferritin H IRE complex (PDB: 3SNP) shown in surface at the same orientation as IRP2 shown in (A).

(C) Superposition of the structures of IRP2 (wheat) and IRP1 (light blue) shown in (A) and (B), respectively.

Figure S6. Structural features of the capping β-strand in FBXL5, Related to Figure 3

(A) Sequence alignment of all FBXL5 LRR β strands and the capping β-strand with three extra flanking residues. The characteristic residues in canonical LRRs are highlighted in yellow. Green arrows indicate the additional two residues that form the horn shown in (C), while the black dot indicates the extra cysteine that forms the tilt shown in (C), which ligates the [2Fe2S] cluster.

(B) Local sequence alignment of FBXL5 orthologs across different species showing the conservation of the three extra residues (boxed) flanking the capping β-strand.

(C) A close-up view of the capping β-strand (slate) in the context of other typical LRRs (teal) in FBXL5.

(D) The capping β-strand (slate) facilitates the formation of a nest-like area at the apical ridge of FBXL5 (teal) to accommodate the [2Fe2S] cluster shown in spheres. The surface representation of the nest-like area is displayed in a view orthogonal to the FBXL5 shown in (C). For clarity, the residues in the utmost C-terminus of FBXL5 are not shown in (C) and (D).

Figure S7. Close-up views of the [2Fe2S] cluster site and its surrounding network, Related to Figures 3 and 4

A series of contacts stabilizing the [2Fe2S] cluster in FBXL5 (teal) and securing the engagement between R779/R763 in IRP2 (wheat) and the interface loop of FBXL5 (teal) are shown in (A) and (B), respectively. The residues involved in these two networks and select residues in the FBXL5 interface loop are shown in sticks, while the [2Fe2S] cluster is shown in spheres. Dashed lines indicate the hydrogen bonds and polar interactions within the networks.

Figure S8. Sequence alignment and structural elements of IRP2, Related to Figure 4

Alignment and secondary structure assignments of IRP2 domain I and II (shown in (A)) and domain IV (shown in (B)) are generated by using sequences of selected orthologs from human (*Homo sapiens*), mouse (*Mus musculus*), bird (*Taeniopygia guttata*), frog (*Xenopus tropicalis*), fish (*Danio rerio*), lancelet (*Branchiostoma belcheri*), and seashell (*Oyster*). The sequence of human IRP1 is also included in the alignment for comparison. Secondary structure elements including α-helices and β-strands are indicated as cylinders and arrows, respectively. Dashed lines represent regions of the protein that are disordered in the solved structure. The 73-amino-acid insertion of IRP2 is shadowed in gray, and the arm helix is labeled correspondingly. Strictly conserved residues are colored black. Green arrows indicate critical FBXL5-binding residues, while black dots indicate the hydrophobic residues in IRP2 that organize the two FBXL5-contacting loops.

Figure S9. A structural model of the IRP2-SCF^{FBXL5} complex, Related to Figure 6

The model is generated on the basis of the known structure of the CUL1-RBX1-SKP1-Fbox complex (PDB: 1LDK) and the solved structure of the IRP2-FBXL5-SKP1 complex in this study.

References

Abbaspour, N., Hurrell, R., and Kelishadi, R. (2014). Review on iron and its importance for human health. J Res Med Sci *19*, 164-174.

Adams, P.D., Afonine, P.V., Bunkoczi, G., Chen, V.B., Davis, I.W., Echols, N., Headd, J.J., Hung, L.W., Kapral, G.J., Grosse-Kunstleve, R.W., *et al.* (2010). PHENIX: a comprehensive Python-based system for macromolecular structure solution. Acta Crystallogr D Biol Crystallogr *66*, 213-221.

Allen, S.J., Giles, K., Gilbert, T., and Bush, M.F. (2016). Ion mobility mass spectrometry of peptide, protein, and protein complex ions using a radio-frequency confining drift cell. Analyst *141*, 884-891.

Anderson, C.P., Shen, M., Eisenstein, R.S., and Leibold, E.A. (2012). Mammalian iron metabolism and its control by iron regulatory proteins. Biochim Biophys Acta *1823*, 1468-1483.

Beard, J.L. (2001). Iron biology in immune function, muscle metabolism and neuronal functioning. J Nutr *131*, 568S-579S; discussion 580S.

Beinert, H., Holm, R.H., and Munck, E. (1997). Iron-sulfur clusters: nature's modular, multipurpose structures. Science *277*, 653-659.

Berrisford, J.M., and Sazanov, L.A. (2009). Structural basis for the mechanism of respiratory complex I. J Biol Chem *284*, 29773-29783.

Chollangi, S., Thompson, J.W., Ruiz, J.C., Gardner, K.H., and Bruick, R.K. (2012). Hemerythrin-like domain within F-box and leucine-rich repeat protein 5 (FBXL5) communicates cellular iron and oxygen availability by distinct mechanisms. J Biol Chem *287*, 23710-23717.

Crielaard, B.J., Lammers, T., and Rivella, S. (2017). Targeting iron metabolism in drug discovery and delivery. Nat Rev Drug Discov *16*, 400-423.

Davidson, K.L., Oberreit, D.R., Hogan, C.J., and Bush, M.F. (2017). Nonspecific aggregation in native electrokinetic nanoelectrospray ionization. Int. J. Mass Spectrom *420*, 35-42.

Dupuy, J., Volbeda, A., Carpentier, P., Darnault, C., Moulis, J.M., and Fontecilla-Camps, J.C. (2006). Crystal structure of human iron regulatory protein 1 as cytosolic aconitase. Structure *14*, 129-139.

Dycke, C., Bougault, C., Gaillard, J., Andrieu, J.P., Pantopoulos, K., and Moulis, J.M. (2007). Human iron regulatory protein 2 is easily cleaved in its specific domain: consequences for the haem binding properties of the protein. Biochem J *408*, 429-439.

Emsley, P., Lohkamp, B., Scott, W.G., and Cowtan, K. (2010). Features and development of Coot. Acta Crystallogr D Biol Crystallogr *66*, 486-501.

Freibert, S.A., Weiler, B.D., Bill, E., Pierik, A.J., Muhlenhoff, U., and Lill, R. (2018). Biochemical Reconstitution and Spectroscopic Analysis of Iron-Sulfur Proteins. Methods Enzymol *599*, 197-226.

Giles, K., Williams, J.P., and Campuzano, I. (2011). Enhancements in travelling wave ion mobility resolution. Rapid Commun Mass Spectrom *25*, 1559-1566.

Grant, T., Rohou, A., and Grigorieff, N. (2018). cisTEM, user-friendly software for single-particle image processing. Elife *7*.

Guo, B., Phillips, J.D., Yu, Y., and Leibold, E.A. (1995). Iron regulates the intracellular degradation of iron regulatory protein 2 by the proteasome. J Biol Chem *270*, 21645-21651.

Haile, D.J., Rouault, T.A., Harford, J.B., Kennedy, M.C., Blondin, G.A., Beinert, H., and Klausner, R.D. (1992). Cellular regulation of the iron-responsive element binding protein: disassembly of the cubane iron-sulfur cluster results in high-affinity RNA binding. Proc Natl Acad Sci U S A *89*, 11735-11739.

Hanson, E.S., Foot, L.M., and Leibold, E.A. (1999). Hypoxia post-translationally activates iron-regulatory protein 2. J Biol Chem *274*, 5047-5052.

Hanson, E.S., Rawlins, M.L., and Leibold, E.A. (2003). Oxygen and iron regulation of iron regulatory protein 2. J Biol Chem *278*, 40337-40342.

Hao, B., Zheng, N., Schulman, B.A., Wu, G., Miller, J.J., Pagano, M., and Pavletich, N.P. (2005). Structural basis of the Cks1-dependent recognition of p27(Kip1) by the SCF(Skp2) ubiquitin ligase. Mol Cell *20*, 9-19.

Hentze, M.W., Muckenthaler, M.U., and Andrews, N.C. (2004). Balancing acts: molecular control of mammalian iron metabolism. Cell *117*, 285-297.

Hentze, M.W., Muckenthaler, M.U., Galy, B., and Camaschella, C. (2010). Two to tango: regulation of Mammalian iron metabolism. Cell *142*, 24-38.

Iwai, K., Klausner, R.D., and Rouault, T.A. (1995). Requirements for iron-regulated degradation of the RNA binding protein, iron regulatory protein 2. EMBO J *14*, 5350-5357.

Kimanius, D., Forsberg, B.O., Scheres, S.H., and Lindahl, E. (2016). Accelerated cryo-EM structure determination with parallelisation using GPUs in RELION-2. Elife *5*.

Kucukelbir, A., Sigworth, F.J., and Tagare, H.D. (2014). Quantifying the local resolution of cryo-EM density maps. Nat Methods *11*, 63-65.

Lieu, P.T., Heiskala, M., Peterson, P.A., and Yang, Y. (2001). The roles of iron in health and disease. Mol Aspects Med *22*, 1-87.

Liu, J., Chakraborty, S., Hosseinzadeh, P., Yu, Y., Tian, S., Petrik, I., Bhagi, A., and Lu, Y. (2014). Metalloproteins containing cytochrome, iron-sulfur, or copper redox centers. Chem Rev *114*, 4366-4469.

Mayank, A.K., Pandey, V., Vashisht, A.A., Barshop, W.D., Rayatpisheh, S., Sharma, T., Haque, T., Powers, D.N., and Wohlschlegel, J.A. (2019). An Oxygen-Dependent Interaction between FBXL5 and the CIA-Targeting Complex Regulates Iron Homeostasis. Mol Cell *75*, 382-393 e385.

Moroishi, T., Nishiyama, M., Takeda, Y., Iwai, K., and Nakayama, K.I. (2011). The FBXL5-IRP2 axis is integral to control of iron metabolism in vivo. Cell Metab *14*, 339-351.

Pettersen, E.F., Goddard, T.D., Huang, C.C., Couch, G.S., Greenblatt, D.M., Meng, E.C., and Ferrin, T.E. (2004). UCSF Chimera--a visualization system for exploratory research and analysis. J Comput Chem *25*, 1605-1612.

Ravid, T., and Hochstrasser, M. (2008). Diversity of degradation signals in the ubiquitin-proteasome system. Nat Rev Mol Cell Biol *9*, 679-690.

Rohou, A., and Grigorieff, N. (2015). CTFFIND4: Fast and accurate defocus estimation from electron micrographs. J Struct Biol *192*, 216-221.

Rosenthal, P.B., and Henderson, R. (2003). Optimal determination of particle orientation, absolute hand, and contrast loss in single-particle electron cryomicroscopy. J Mol Biol *333*, 721-745.

Rouault, T.A. (2006). The role of iron regulatory proteins in mammalian iron homeostasis and disease. Nat Chem Biol *2*, 406-414.

Salahudeen, A.A., Thompson, J.W., Ruiz, J.C., Ma, H.W., Kinch, L.N., Li, Q., Grishin, N.V., and Bruick, R.K. (2009). An E3 ligase possessing an iron-responsive hemerythrin domain is a regulator of iron homeostasis. Science *326*, 722-726.

Shu, C., Sung, M.W., Stewart, M.D., Igumenova, T.I., Tan, X., and Li, P. (2012). The structural basis of iron sensing by the human F-box protein FBXL5. Chembiochem *13*, 788-791.

Shubin, A.A., and Dikanov, S.A. (2006). Variations of g-tensor principal values in reduced [2Fe−2S] cluster of iron-sulfur proteins. Appl. Magn. Reson *30*, 399-416.

Stoll, S., and Schweiger, A. (2006). EasySpin, a comprehensive software package for spectral simulation and analysis in EPR. J Magn Reson *178*, 42-55.

Suloway, C., Pulokas, J., Fellmann, D., Cheng, A., Guerra, F., Quispe, J., Stagg, S., Potter, C.S., and Carragher, B. (2005). Automated molecular microscopy: the new Leginon system. J Struct Biol *151*, 41-60.

Tan, M.K., Lim, H.J., Bennett, E.J., Shi, Y., and Harper, J.W. (2013). Parallel SCF adaptor capture proteomics reveals a role for SCFFBXL17 in NRF2 activation via BACH1 repressor turnover. Mol Cell *52*, 9-24.

Thompson, J.W., and Bruick, R.K. (2012). Protein degradation and iron homeostasis. Biochim Biophys Acta *1823*, 1484-1490.

Thompson, J.W., Salahudeen, A.A., Chollangi, S., Ruiz, J.C., Brautigam, C.A., Makris, T.M., Lipscomb, J.D., Tomchick, D.R., and Bruick, R.K. (2012). Structural and molecular characterization of iron-sensing hemerythrin-like domain within F-box and leucine-rich repeat protein 5 (FBXL5). J Biol Chem *287*, 7357-7365.

Tong, W.H., and Rouault, T.A. (2006). Functions of mitochondrial ISCU and cytosolic ISCU in mammalian iron-sulfur cluster biogenesis and iron homeostasis. Cell Metab *3*, 199-210.

Vashisht, A.A., Zumbrennen, K.B., Huang, X., Powers, D.N., Durazo, A., Sun, D., Bhaskaran, N., Persson, A., Uhlen, M., Sangfelt, O.*, et al.* (2009). Control of iron homeostasis by an iron-regulated ubiquitin ligase. Science *326*, 718-721.

Walden, W.E., Selezneva, A.I., Dupuy, J., Volbeda, A., Fontecilla-Camps, J.C., Theil, E.C., and Volz, K. (2006). Structure of dual function iron regulatory protein 1 complexed with ferritin IRE-RNA. Science *314*, 1903-1908.

Wallander, M.L., Leibold, E.A., and Eisenstein, R.S. (2006). Molecular control of vertebrate iron homeostasis by iron regulatory proteins. Biochim Biophys Acta *1763*, 668-689.

Wang, J., Chen, G., Lee, J., and Pantopoulos, K. (2008). Iron-dependent degradation of IRP2 requires its C-terminal region and IRP structural integrity. BMC Mol Biol *9*, 15.

Xing, W., Busino, L., Hinds, T.R., Marionni, S.T., Saifee, N.H., Bush, M.F., Pagano, M., and Zheng, N. (2013). SCF(FBXL3) ubiquitin ligase targets cryptochromes at their cofactor pocket. Nature *496*, 64-68.

Ye, H., Jeong, S.Y., Ghosh, M.C., Kovtunovych, G., Silvestri, L., Ortillo, D., Uchida, N., Tisdale, J., Camaschella, C., and Rouault, T.A. (2010). Glutaredoxin 5 deficiency causes sideroblastic anemia by specifically impairing heme biosynthesis and depleting cytosolic iron in human erythroblasts. J Clin Invest *120*, 1749-1761.

Zhang, K. (2016). Gctf: Real-time CTF determination and correction. J Struct Biol *193*, 1-12.

Zheng, N., and Shabek, N. (2017). Ubiquitin Ligases: Structure, Function, and Regulation. Annu Rev Biochem *86*, 129-157.

Zheng, S.Q., Palovcak, E., Armache, J.P., Verba, K.A., Cheng, Y., and Agard, D.A. (2017). MotionCor2: anisotropic correction of beam-induced motion for improved cryo-electron microscopy. Nat Methods *14*, 331-332.

Zivanov, J., Nakane, T., Forsberg, B.O., Kimanius, D., Hagen, W.J., Lindahl, E., and Scheres, S.H. (2018). New tools for automated high-resolution cryo-EM structure determination in RELION-3. Elife *7*.

Zivanov, J., Nakane, T., and Scheres, S.H.W. (2019). A Bayesian approach to beam-induced motion correction in cryo-EM single-particle analysis. IUCrJ *6*, 5-17.

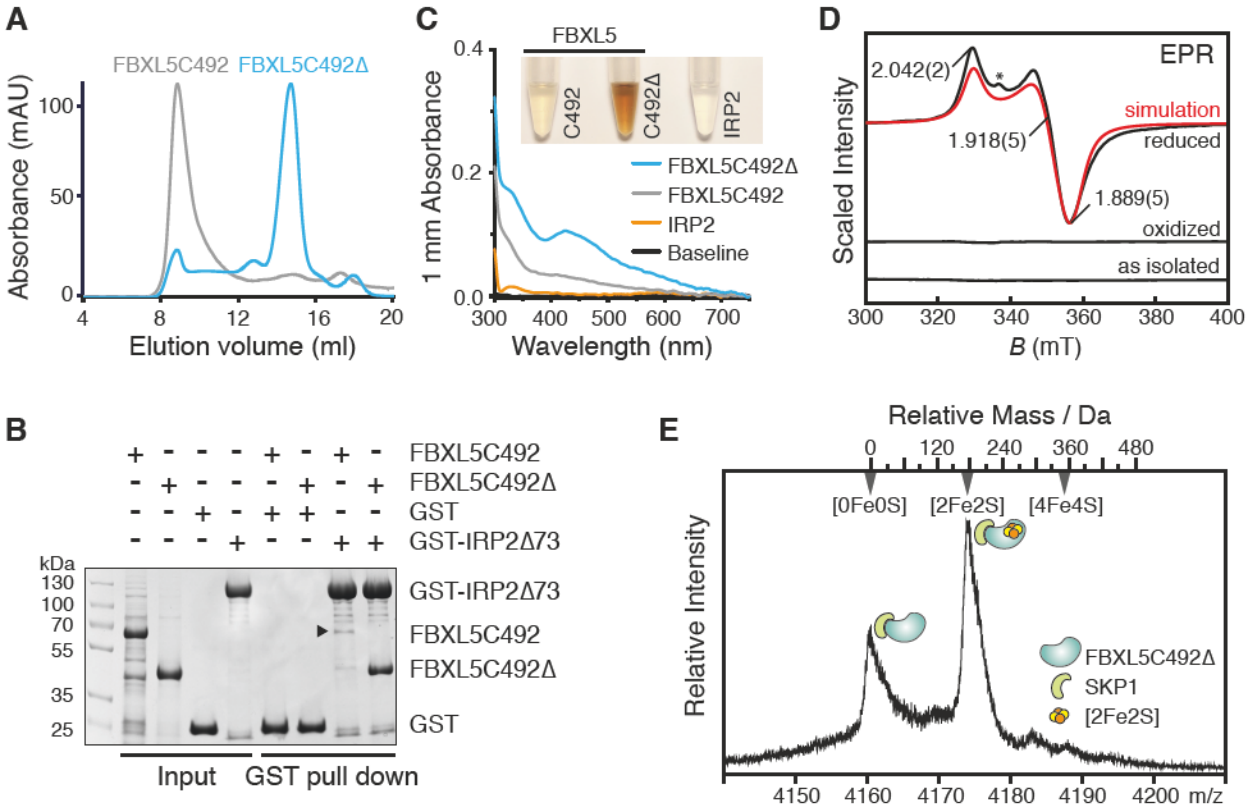
A
FBXL5C492
FBXL5C492Δ
Absorbance (mAU)
Elution volume (ml)
B
FBXL5C492
FBXL5C492Δ
GST
GST-IRP2Δ73
kDa
130
100
70
55
35
25
GST-IRP2Δ73
FBXL5C492
FBXL5C492Δ
GST
Input
GST pull down
C
FBXL5
C492
C492Δ
IRP2
1 mm Absorbance
Wavelength (nm)
FBXL5C492Δ
FBXL5C492
IRP2
Baseline
D
EPR
2.042(2)
1.918(5)
1.889(5)
simulation
reduced
oxidized
as isolated
Scaled Intensity
B (mT)
E
Relative Mass / Da
[0Fe0S]
[2Fe2S]
[4Fe4S]
Relative Intensity
FBXL5C492Δ
SKP1
[2Fe2S]
m/z

Figure 1

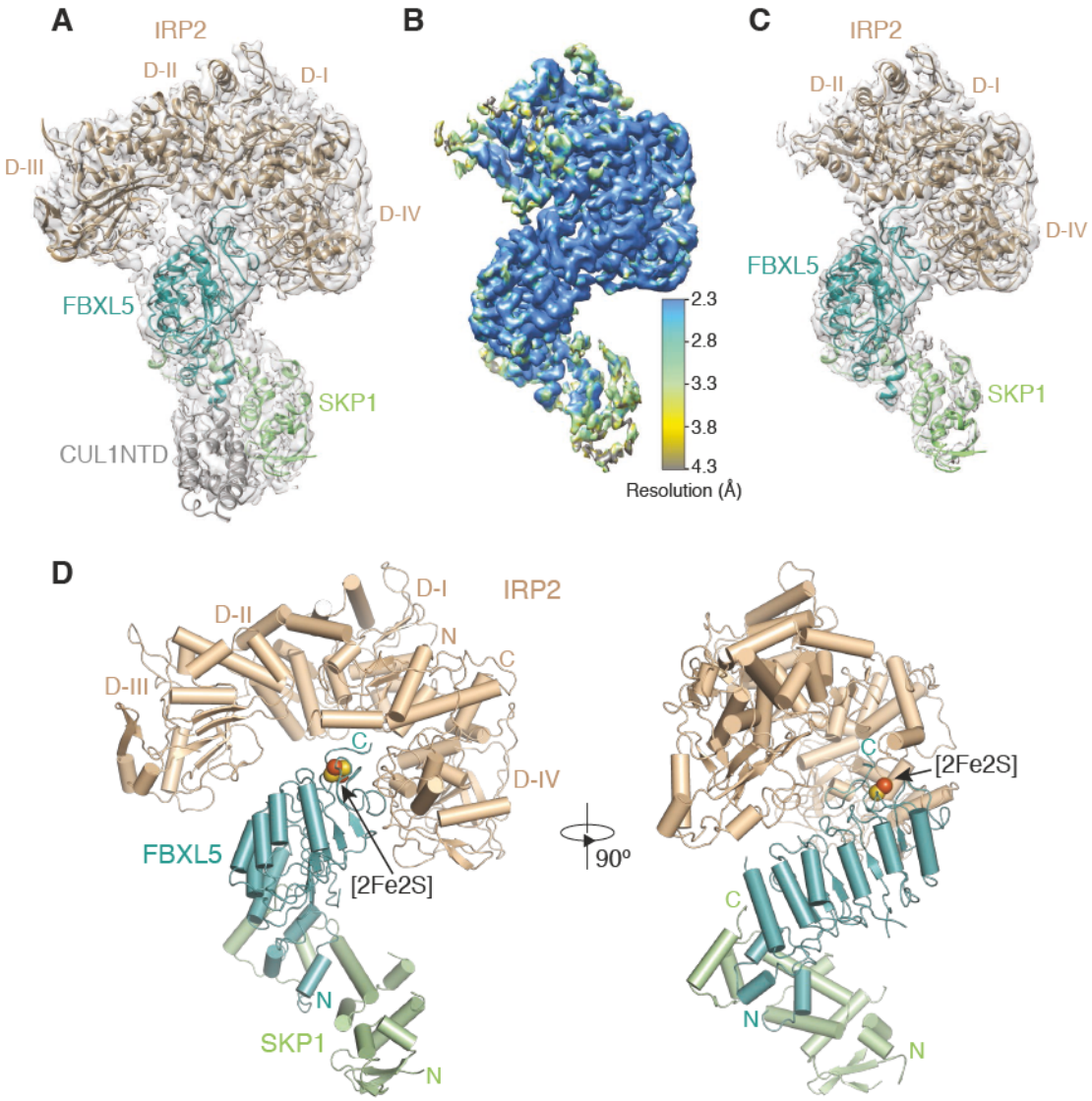
A
IRP2
D-II
D-I
D-III
D-IV
FBXL5
SKP1
CUL1NTD
B
2.3
2.8
3.3
3.8
4.3
Resolution (Å)
C
IRP2
D-II
D-I
D-IV
FBXL5
SKP1
D
IRP2
D-I
D-II
N
C
D-III
C
D-IV
FBXL5
[2Fe2S]
N
SKP1
N
90º
C
[2Fe2S]
C
N
N

Figure 2

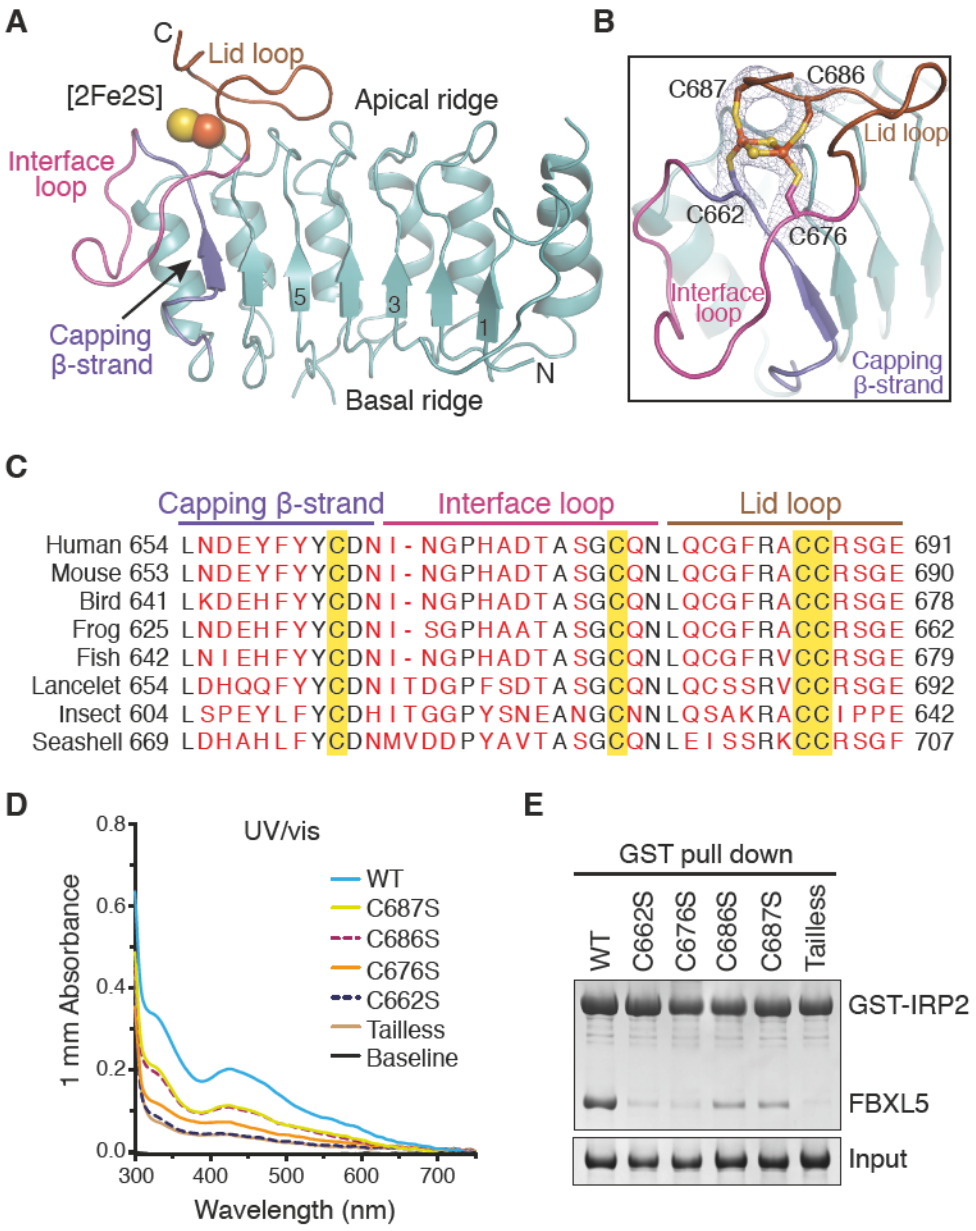
A
C
Lid loop
[2Fe2S]
Apical ridge
Interface loop
Capping β-strand
5
1
3
1
N
Basal ridge
B
C687
C686
Lid loop
C662
C676
Interface loop
Capping β-strand
C
Capping β-strand
Interface loop
Lid loop
Human 654 LNDEYFYYCDNI-NGPHADTASGCQNLQCGFRACCRSGE 691
Mouse 653 LNDEYFYYCDNI-NGPHADTASGCQNLQCGFRACCRSGE 690
Bird 641 LKDEHFYYCDNI-NGPHADTASGCQNLQCGFRACCRSGE 678
Frog 625 LNDEHFYYCDNI-SGPHAATASGCQNLQCGFRACCRSGE 662
Fish 642 LNIEHFYYCDNI-NGPHADTASGCQNLQCGFRVCCRSGE 679
Lancelet 654 LDHQQFYYCDNITDGPFSDTASGCQNLQCSSRVCCRSGE 692
Insect 604 LSPEYLFYCDHITGGPYSNEANGCNNLQSAKRACCIPPE 642
Seashell 669 LDHAHLFYCDNMVDDPYAVTASGCQNLEISSRKCCRSGF 707
D
UV/vis
1 mm Absorbance
0.8
0.6
0.4
0.2
0.0
300
400
500
600
700
Wavelength (nm)
WT
C687S
C686S
C676S
C662S
Tailless
Baseline
E
GST pull down
WT
C662S
C676S
C686S
C687S
Tailless
GST-IRP2
FBXL5
Input

Figure 3

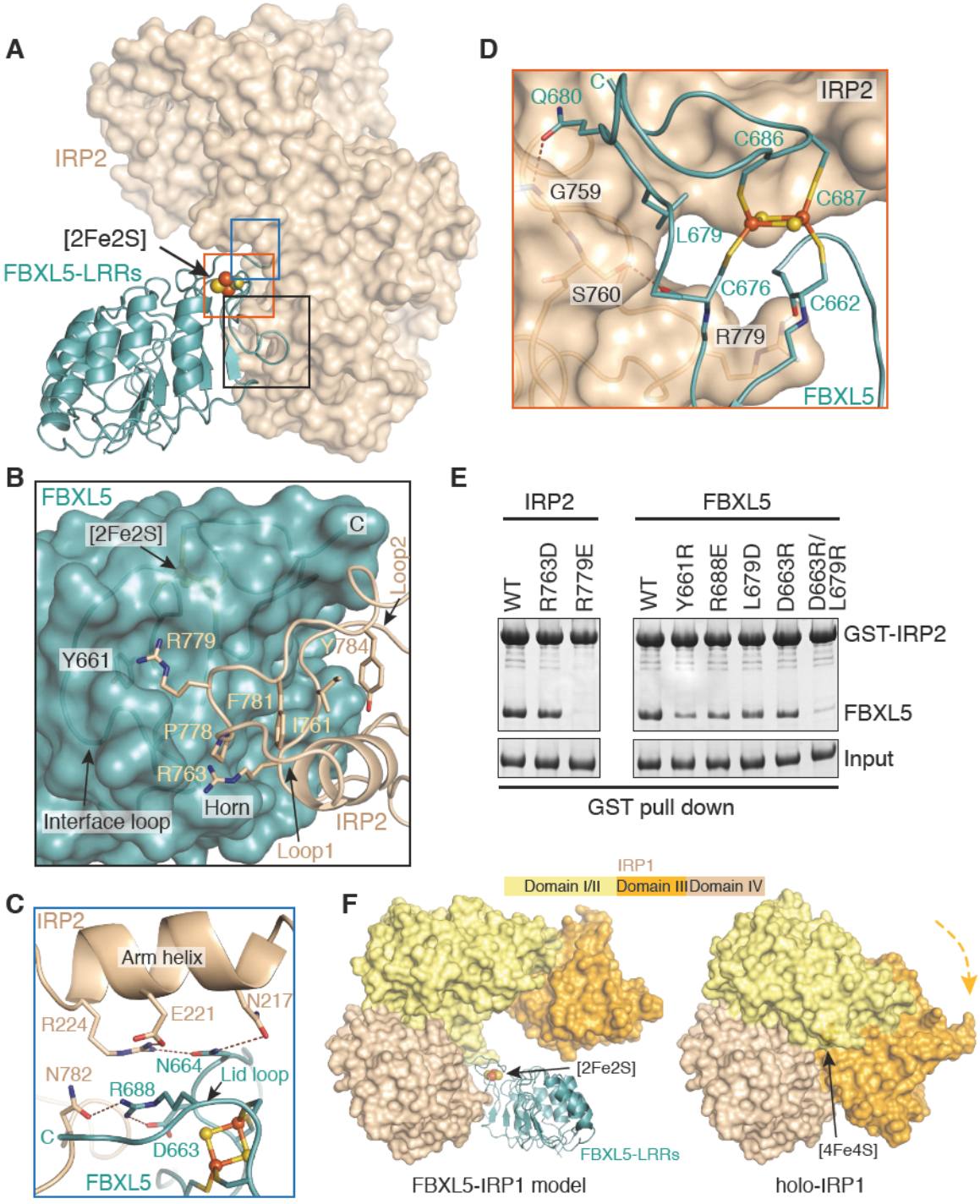
A
IRP2
[2Fe2S]
FBXL5-LRRs
D
IRP2
Q680
C
C686
G759
C687
L679
S760
C676
C662
R779
FBXL5
B
FBXL5
[2Fe2S]
C
Loop2
R779
Y784
Y661
F781
P778
I761
R763
Horn
Interface loop
IRP2
Loop1
E
IRP2
FBXL5
WT
R763D
R779E
WT
Y661R
R688E
L679D
D663R
D663R/
L679R
GST-IRP2
FBXL5
Input
GST pull down
C
IRP2
Arm helix
N217
E221
R224
N664
N782
Lid loop
R688
C
D663
FBXL5
F
IRP1
Domain I/II
Domain III
Domain IV
[2Fe2S]
FBXL5-LRRs
[4Fe4S]
FBXL5-IRP1 model
holo-IRP1

Figure 4

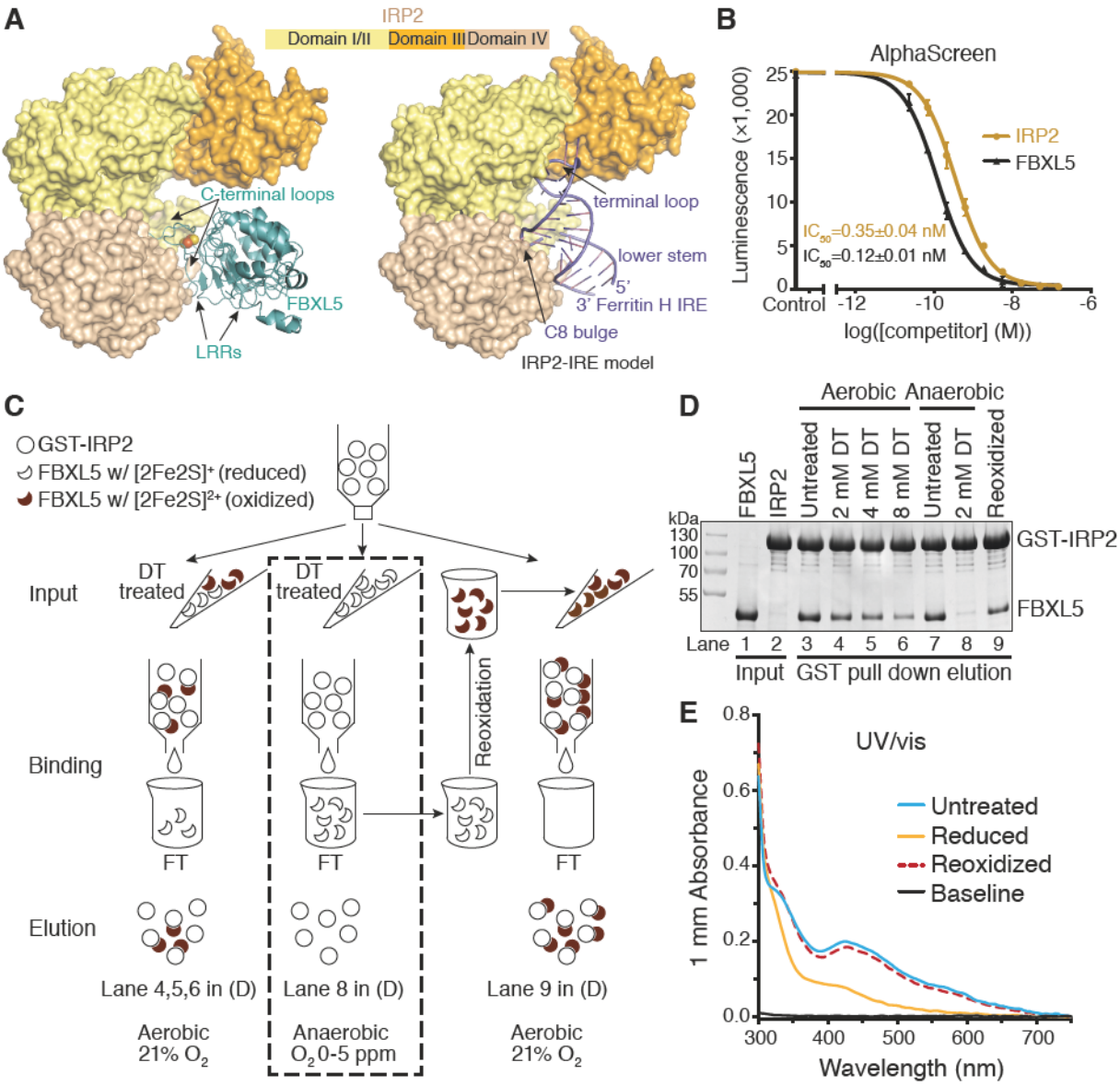
A
IRP2
Domain I/II
Domain III
Domain IV
C-terminal loops
FBXL5
LRRs
terminal loop
lower stem
5'
3' Ferritin H IRE
C8 bulge
IRP2-IRE model
B
AlphaScreen
Luminescence (×1,000)
IRP2
FBXL5
IC50=0.35±0.04 nM
IC50=0.12±0.01 nM
Control
log([competitor] (M))
C
GST-IRP2
FBXL5 w/ [2Fe2S]+ (reduced)
FBXL5 w/ [2Fe2S]2+ (oxidized)
Input
DT treated
Binding
Reoxidation
FT
Elution
Lane 4,5,6 in (D)
Lane 8 in (D)
Lane 9 in (D)
Aerobic 21% O2
Anaerobic O2 0-5 ppm
Aerobic 21% O2
D
Aerobic
Anaerobic
FBXL5
IRP2
Untreated
2 mM DT
4 mM DT
8 mM DT
Untreated
2 mM DT
Reoxidized
kDa
130
100
70
55
GST-IRP2
FBXL5
Lane 1 2 3 4 5 6 7 8 9
Input
GST pull down elution
E
UV/vis
1 mm Absorbance
Untreated
Reduced
Reoxidized
Baseline
Wavelength (nm)

Figure 5

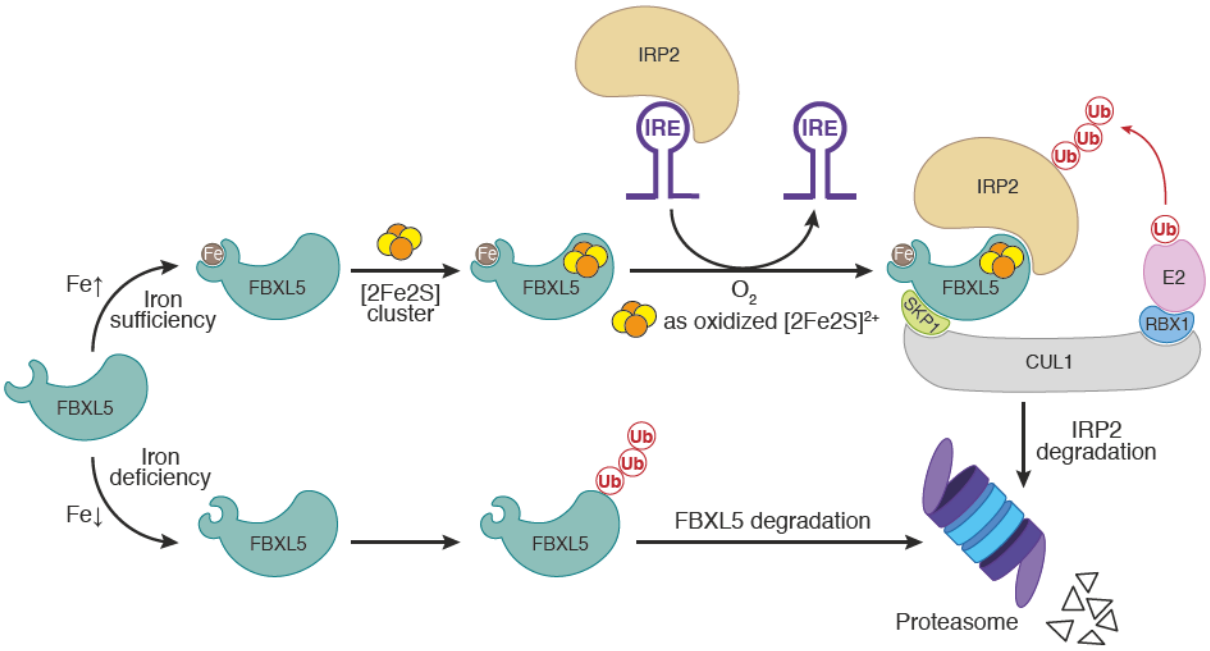
IRP2
IRE
IRE
Ub
Ub
Ub
IRP2
Fe
FBXL5
Fe↑
Iron
sufficiency
[2Fe2S]
cluster
Fe
FBXL5
O2
as oxidized [2Fe2S]2+
Fe
FBXL5
SKP1
E2
RBX1
CUL1
FBXL5
IRP2
degradation
Iron
deficiency
Fe↓
FBXL5
Ub
Ub
Ub
FBXL5
FBXL5 degradation
Proteasome

Figure 6

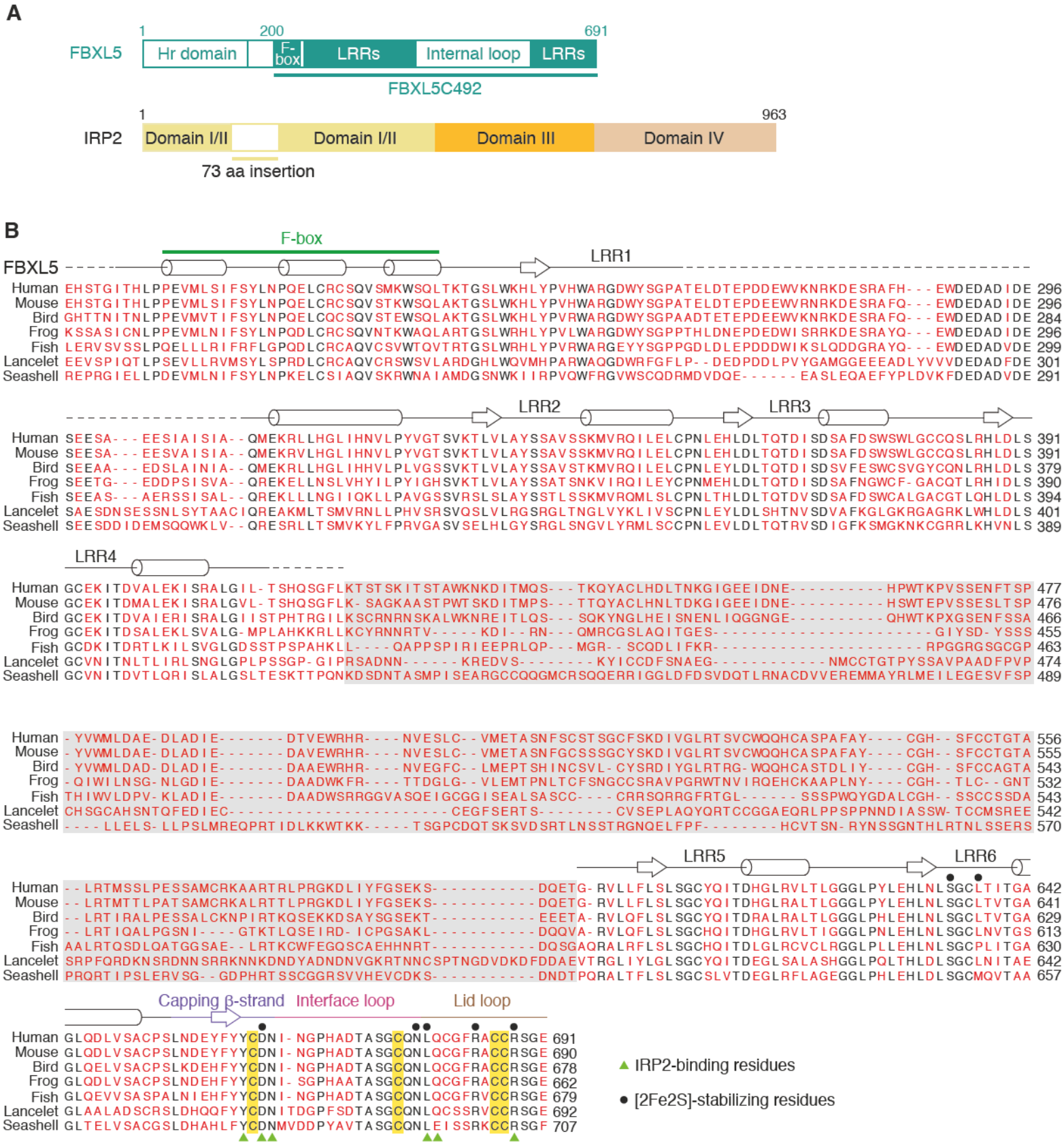
A
FBXL5
1
200
691
Hr domain
F-box
LRRs
Internal loop
LRRs
FBXL5C492
IRP2
1
963
Domain I/II
Domain I/II
Domain III
Domain IV
73 aa insertion
B
F-box
FBXL5
LRR1
LRR2
LRR3
LRR4
LRR5
LRR6
Capping β-strand
Interface loop
Lid loop
Human
Mouse
Bird
Frog
Fish
Lancelet
Seashell
IRP2-binding residues
[2Fe2S]-stabilizing residues

Figure S1

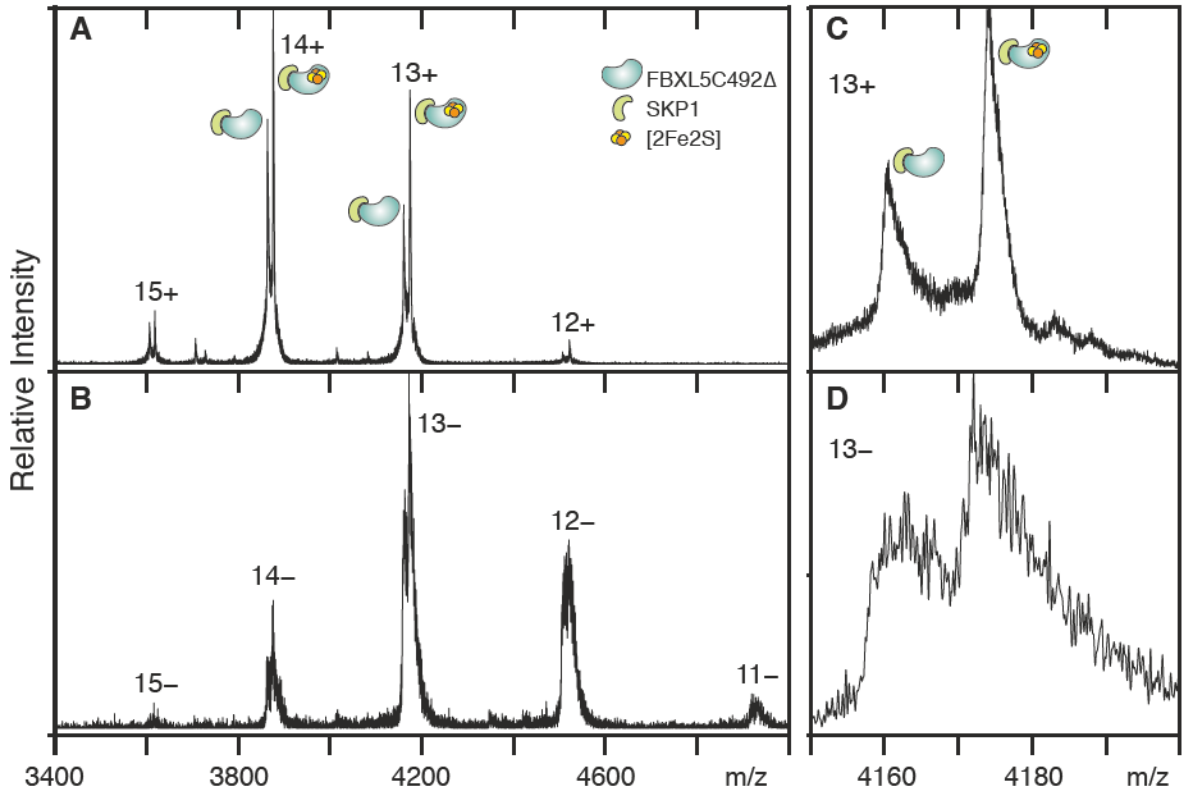
A
14+
13+
15+
12+
FBXL5C492Δ
SKP1
[2Fe2S]
B
13–
14–
12–
15–
11–
Relative Intensity
3400
3800
4200
4600
m/z
C
13+
D
13–
4160
4180
m/z

Figure S2

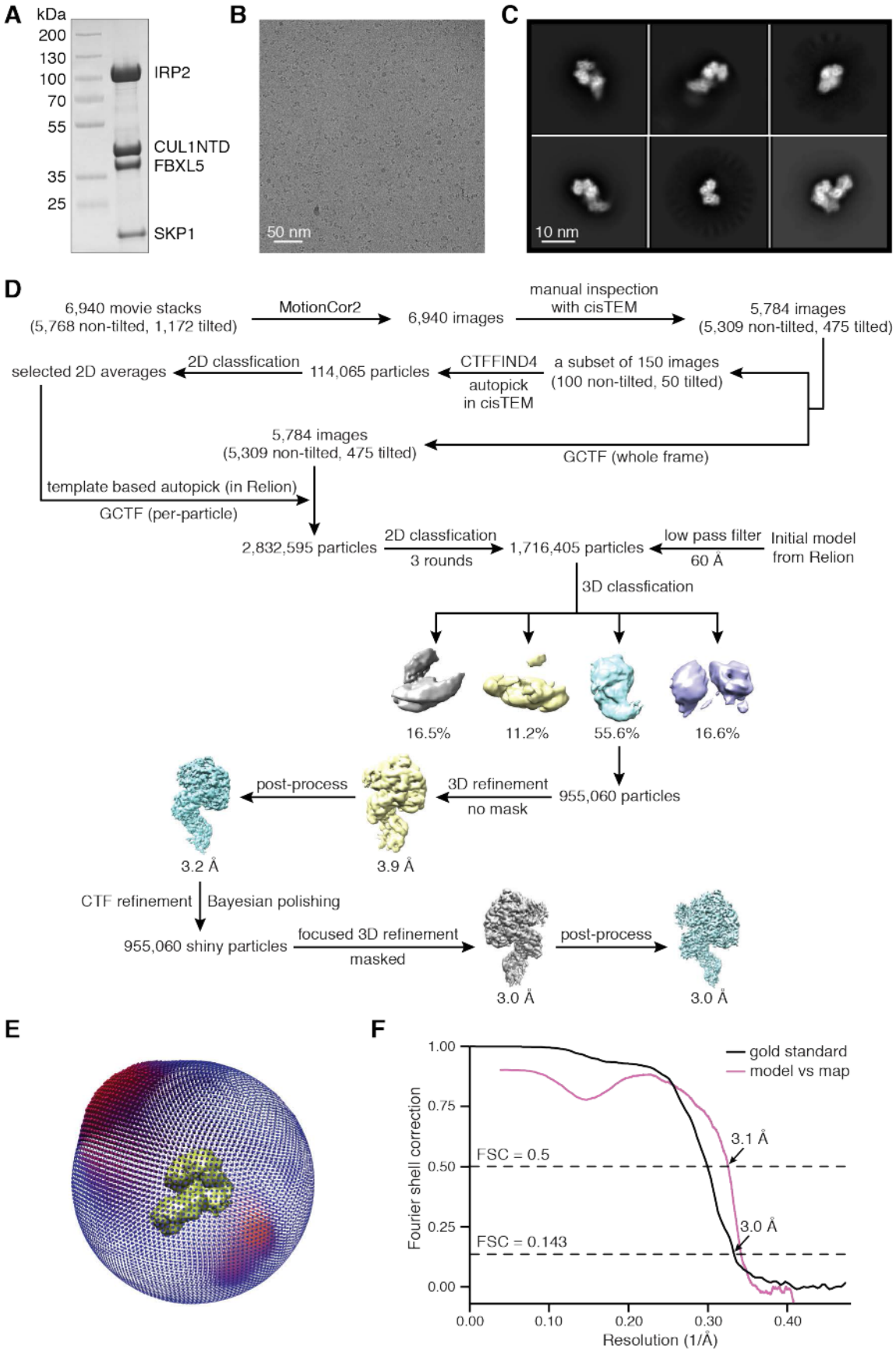
A
kDa
200
130
100
70
55
35
25
IRP2
CUL1NTD
FBXL5
SKP1
B
50 nm
C
10 nm
D
6,940 movie stacks
(5,768 non-tilted, 1,172 tilted)
MotionCor2
6,940 images
manual inspection
with cisTEM
5,784 images
(5,309 non-tilted, 475 tilted)
a subset of 150 images
(100 non-tilted, 50 tilted)
CTFFIND4
autopick
in cisTEM
114,065 particles
2D classfication
selected 2D averages
5,784 images
(5,309 non-tilted, 475 tilted)
GCTF (whole frame)
template based autopick (in Relion)
GCTF (per-particle)
2,832,595 particles
2D classfication
3 rounds
1,716,405 particles
low pass filter
60 Å
Initial model
from Relion
3D classfication
16.5%
11.2%
55.6%
16.6%
955,060 particles
3D refinement
no mask
post-process
3.9 Å
3.2 Å
CTF refinement
Bayesian polishing
955,060 shiny particles
focused 3D refinement
masked
post-process
3.0 Å
3.0 Å
E
F
gold standard
model vs map
Fourier shell correction
1.00
0.75
0.50
0.25
0.00
FSC = 0.5
FSC = 0.143
3.1 Å
3.0 Å
0.00
0.10
0.20
0.30
0.40
Resolution (1/Å)

Figure S3

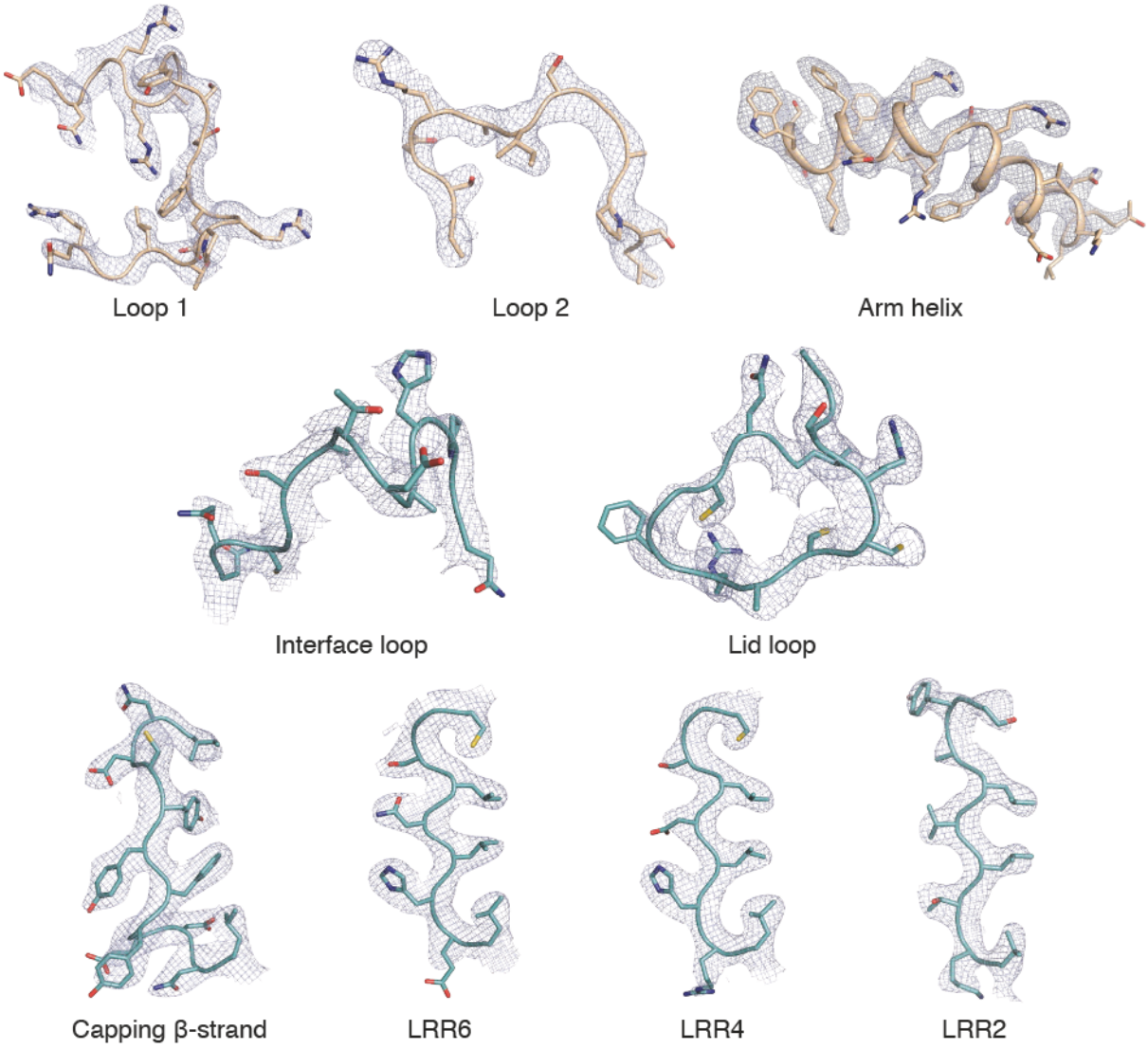
Loop 1
Loop 2
Arm helix
Interface loop
Lid loop
Capping β-strand
LRR6
LRR4
LRR2

Figure S4

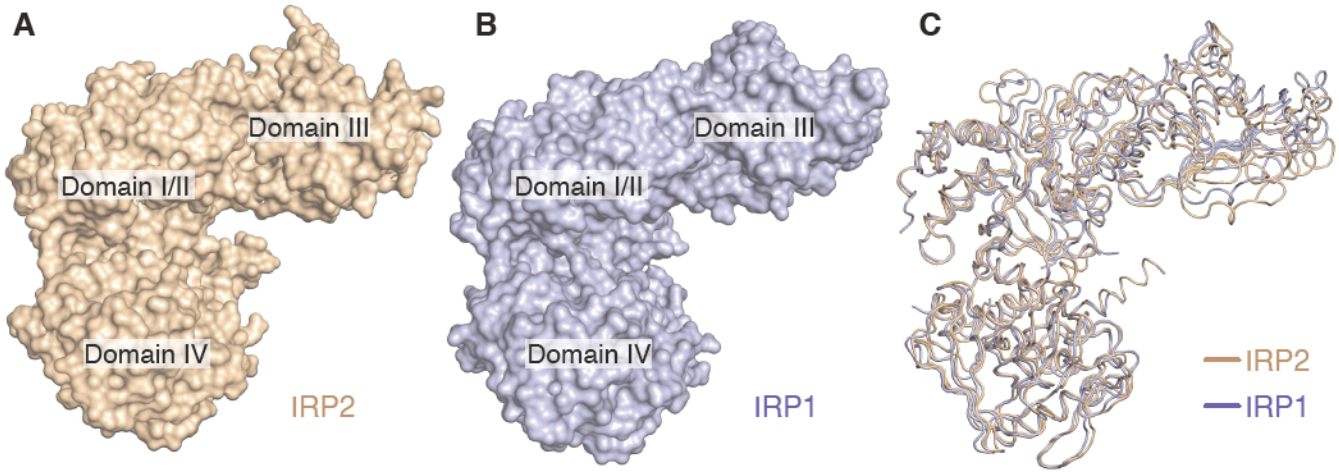
A
Domain III
Domain I/II
Domain IV
IRP2
B
Domain III
Domain I/II
Domain IV
IRP1
C
IRP2
IRP1

Figure S5

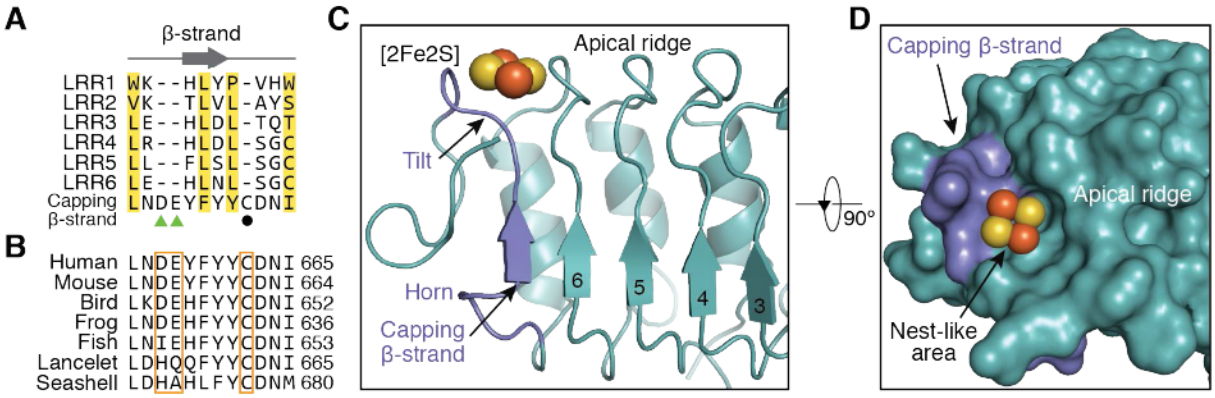
A
β-strand
LRR1 WK--HLYP-VHW
LRR2 VK--TLVL-AYS
LRR3 LE--HLDL-TQT
LRR4 LR--HLDL-SGC
LRR5 LL--FLSL-SGC
LRR6 LE--HLNL-SGC
Capping β-strand LNDEYFYYCDNI
B
Human LNDEYFYYCDNI 665
Mouse LNDEYFYYCDNI 664
Bird LKDEHFYYCDNI 652
Frog LNDEHFYYCDNI 636
Fish LNIEHFYYCDNI 653
Lancelet LDHQQFYYCDNI 665
Seashell LDHAHLFYCDNM 680
C
[2Fe2S]
Apical ridge
Tilt
Horn
Capping β-strand
6
5
4
3
90°
D
Capping β-strand
Apical ridge
Nest-like area

Figure S6

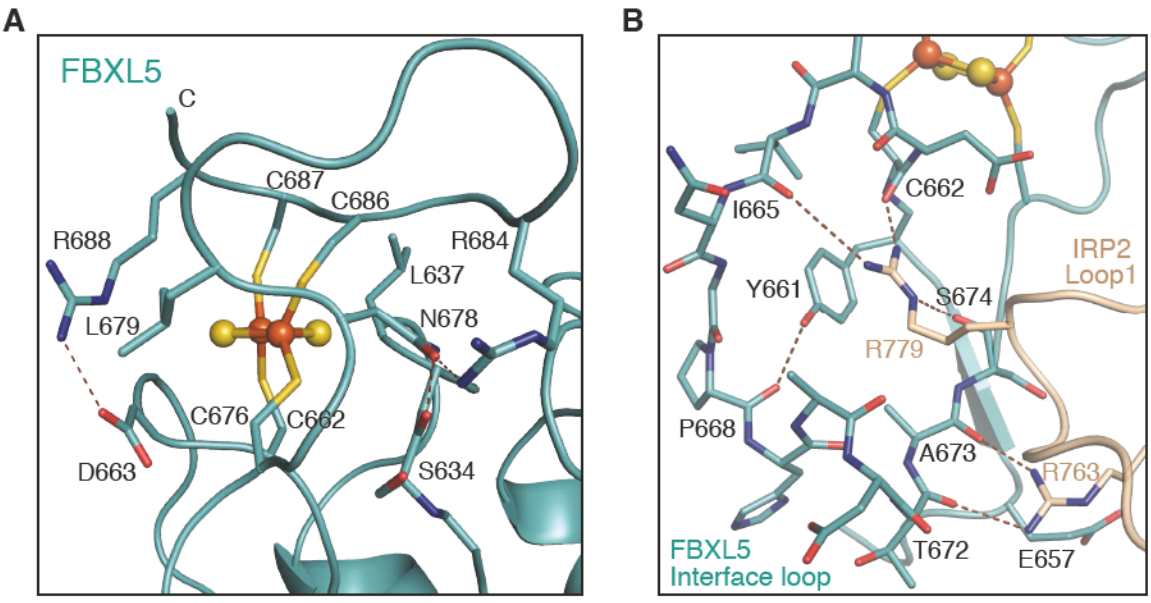
A
FBXL5
C
C687
C686
R688
R684
L637
L679
N678
C676
C662
D663
S634
B
C662
I665
IRP2
Loop1
Y661
S674
R779
P668
A673
R763
FBXL5
Interface loop
T672
E657

Figure S7

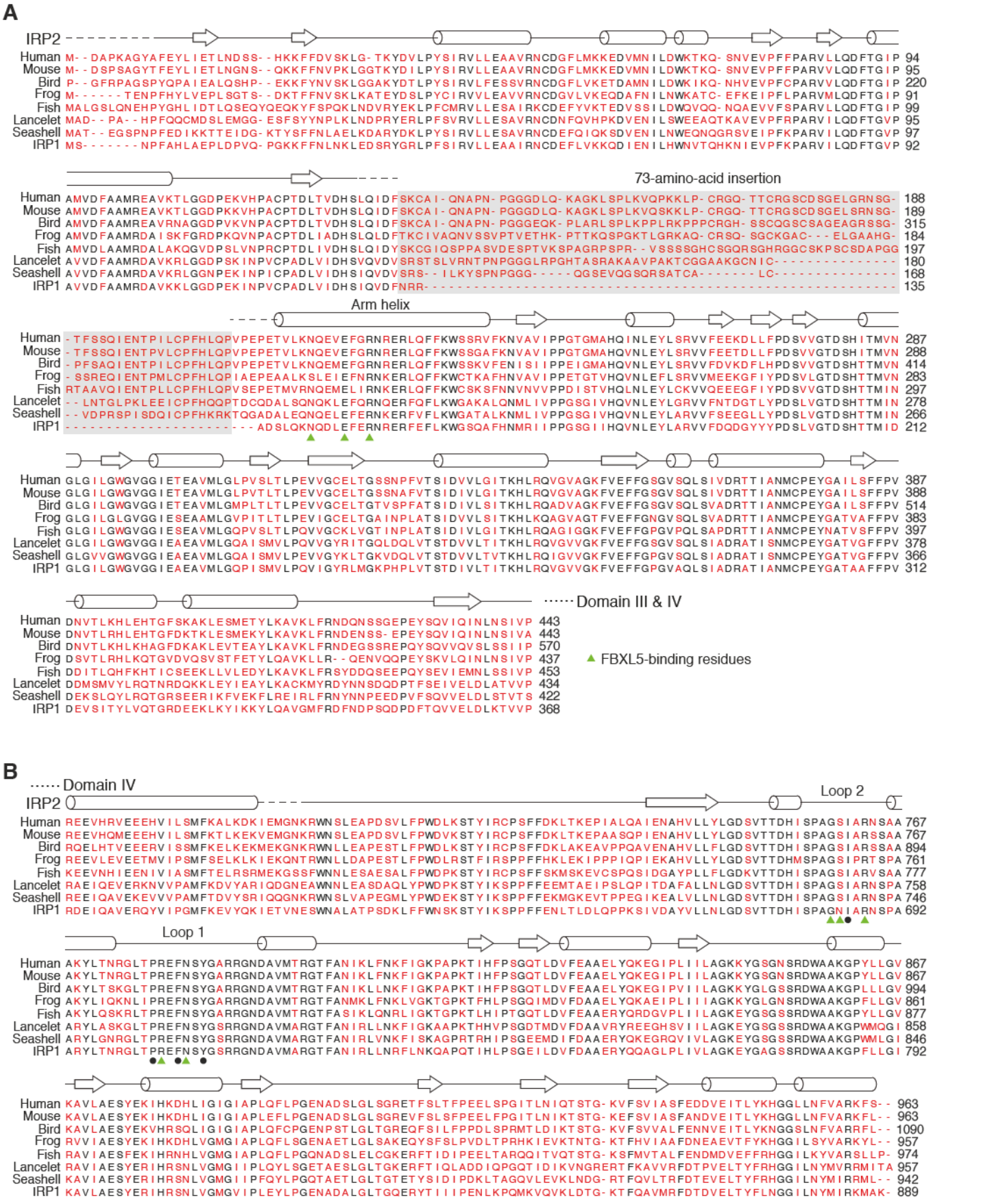
A
IRP2
Human
Mouse
Bird
Frog
Fish
Lancelet
Seashell
IRP1
73-amino-acid insertion
Arm helix
Domain III & IV
FBXL5-binding residues
B
Domain IV
Loop 2
Loop 1
FBXL5-binding residues
Hydrophobic packing residues in self-organization

Figure S8

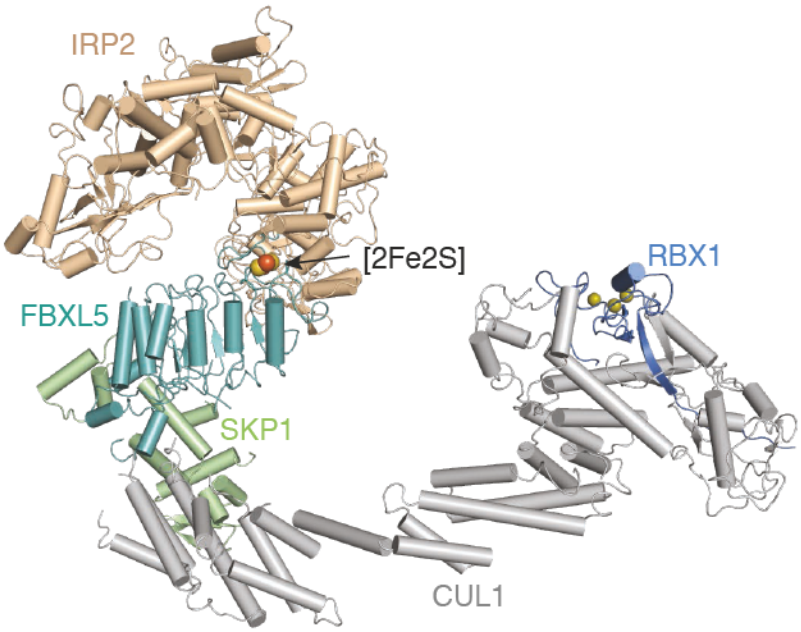

Figure S9

Table S1. Cryo-EM data collection, refinement and validation statistics, Related to Figure 2

	IRP2-FBXL5-SKP1
Data collection and processing	
Microscope	Titan Krios
Detector	K2 Summit
Magnification	130,000
Voltage (kV)	300
Electron exposure (e–/Å^2)	73.8
Defocus range (μm)	1.5 to 3
Pixel size (Å)	1.056 (physical)
Symmetry imposed	C1
Initial particle images (no.)	2,832,595
Final particle images (no.)	955,060
Resolution at 0.143 FSC threshold (Å)	3.0
Map resolution range (Å)	2.3-4.0
Refinement	
Resolution at 0.5 FSC threshold (Å)	3.1
Map sharpening *B* factor (Å^2)	-78
Model composition	
Non-hydrogen atoms	8082
Protein residues	1033
[2Fe2S]	1
B-factors (Å^2)	
Protein	41.74
[2Fe2S]	23.88
R.M.S. deviations	
Bond lengths (Å)	0.005
Bond angles (°)	0.644
Validation	
MolProbity score	2.05
Clashscore	9.28
Rotamer outliers (%)	0.11
CaBLAM outliers (%)	4.73
EMRinger score	3.72
Ramachandran plot	
Favored (%)	90.23
Allowed (%)	9.77
Outliers (%)	0